

Theory of Super-Resolution Data Assimilation with Conditional Variational Autoencoders: Using Super-Resolution Operators as Background Error Covariance Matrices

Yuki Yasuda¹ and Ryo Onishi¹

*Supercomputing Research Center, Institute of Integrated Research,
Institute of Science Tokyo, 2-12-1 Ookayama, Meguro-ku, Tokyo 1528550,
Japan*

(*Electronic mail: onishi.ryo@gsic.titech.ac.jp)

(*Electronic mail: yasuda.y.25d8@m.isct.ac.jp)

(Dated: 4 October 2024)

This study proposes a theory of unsupervised super-resolution data assimilation (SRDA) using conditional variational autoencoders (CVAEs). This framework employs an evidence lower bound as the objective function and encompasses the three-dimensional variational (3D-Var) formalism. Similar to 3D-Var, it is essential to use a non-diagonal background error covariance matrix to assimilate distant observations. Instead of using such a non-diagonal matrix, we extend the proposed framework to employ the non-local nature of super-resolution operations. In the extended framework, super-resolution operators can serve as background error covariance matrices. Since the loss function for CVAEs is generally an evidence lower bound, SRDA can be performed using CVAEs. By incorporating the SR model into the CVAE, the encoder estimates the high-resolution (HR) analysis from the input of HR observations and low-resolution (LR) forecasts, while the decoder acts as the observation operator and reconstructs the HR observations from the estimated HR analysis. The effectiveness of the proposed method was evaluated through numerical experiments using an idealized barotropic ocean jet system. Compared to inference by an ensemble Kalman filter, the proposed SRDA demonstrated its ability to obtain accurate HR inferences within shorter computational times because the SRDA does not require HR numerical integration or ensemble calculations. The findings of this study provide a theoretical basis for the fusion of SR and DA, which will stimulate further research on their integration.

I. INTRODUCTION

Data assimilation (DA) is an essential technique for various modeling in computational fluid dynamics (CFD).^{1,2} Fluid systems generally exhibit chaotic behavior, where errors in initial conditions grow over time. Uncertainties in model parameters can also lead to discrepancies from reality. DA reduces these errors by correcting forecast values or model parameters based on observational data, thereby being essential for accurate predictions.

Recent advances in deep learning are impacting various scientific fields and are also found in DA. One reason is that both DA and deep learning use backpropagation based on adjoint equations.³⁻⁵ Another reason stems from the use of the Bayesian approach.^{2,5,6} In this approach, computational processes for target variables are modeled by probability distributions based on known data. For instance, in image generation,^{7,8} image data distributions are modeled and learned from existing images. Once trained, the neural network can generate a new image by sampling from the learned distribution. In DA, the true states of fluid systems are estimated through Bayesian modeling, namely by integrating known data, such as observations and fluid model outputs.

A typical neural network based on the Bayesian approach is the variational autoencoder (VAE).^{7,9,10} Like standard autoencoders,¹¹ a VAE consists of an encoder and a decoder, both of which are implemented by neural networks. Typically, the encoder transforms the input data into a compressed representation in the latent space, while the decoder reconstructs the original data from these latent variables. The integration of Bayesian inference introduces two key characteristics into VAEs.^{7,9,10} First, a regularization term is added to the loss function, which structures the latent space. For instance, in a problem of generating handwritten digits, a specific dimension in the latent space may govern the digit styles.^{9,10} Second, the VAE acts as a generative model and can produce new data by sampling a latent variable and decoding it. The Conditional VAE (CVAE) is an extension of VAEs that is based on conditional probability modeling.^{12,13} In the problem of handwritten digits, for example, CVAEs make it feasible to designate handwritten digits to be generated through this conditioning.^{12,13}

Applications of VAEs in DA can be categorized into two groups. The first group employs VAEs for dimensionality reduction.¹⁴⁻¹⁶ In this approach, the encoder maps fluid model states into a low-dimensional latent space. DA methods, such as Kalman filters, are then applied in this space. Due to the reduced dimensionality, the computational cost is significantly lowered.

This scheme is referred to as latent DA and has been extensively studied using various encoder-decoder networks.^{17–19} The second group employs VAEs as generators that learn the probability distribution of flow fields.^{20–22} In this scheme, a fluid model state (i.e., a background state) is first encoded. Noise is then added in the latent space, creating various potential latent variables. Ensemble members are finally obtained by decoding these latent variables back into the physical space. This process facilitates efficient computation of covariance matrices used in DA methods, such as Kalman filters. A common characteristic in both groups is that VAEs do not directly perform DA; rather, VAEs are used to make DA methods more efficient. The present study proposes a new method, categorized into the third group, where VAEs directly perform DA.

In statistical DA methods, such as Kalman filters, the estimation of background error covariance matrices is essential for inferring the true state.^{1,2} Typically, observations represent a state close to reality, but they are spatially sparse. In contrast, fluid model outputs (i.e., background states) include larger errors, but they are spatially dense. In DA, these background states are corrected by observations in a non-local manner using covariance matrices. For instance, when an observed value exists at a grid point, this observation is used to correct surrounding background values that are correlated with the background at that point.

The estimation of covariance matrices is also important for DA using autoencoders (including VAEs). In latent DA, the covariance structure needs to be estimated because the statistics of the latent space are typically unknown.^{16,18} More generally, the background error distributions are non-Gaussian, and such statistics can be estimated by VAEs.²³ The distributions learned by VAEs can be incorporated into a traditional DA method,²³ namely the three-dimensional variational (3D-Var)²⁴ formalism. In the present study, we focus on the non-local nature of super-resolution (SR) and utilize SR operators as covariance matrices.

Originally, SR is a technique to enhance the resolution of images and has been studied in computer vision as an application of neural networks.^{25,26} The success of such neural networks has led to numerous applications of SR in fluid dynamics,^{27–35} as reviewed in a recent survey.³⁶ An important characteristic of SR is its non-local nature, where SR neural networks map low-resolution (LR) patterns with a certain spatial extent to high-resolution (HR) patterns.^{37,38} Neural networks can focus on input LR patterns that are similar or spatially correlated to the target HR patterns, generating high-quality HR images using the non-local information in the input.³⁸

Recently, SR has been integrated into DA, referred to as super-resolution data assimilation (SRDA).^{39,40} One reason for this integration is the increasing availability of HR observations.^{41–43}

In typical DA methods, HR observations are assimilated into HR background states from HR fluid models,^{44,45} which require a large amount of computational resources for time integration. In contrast, in SRDA frameworks, background states are computed with LR fluid models. The LR results are then super-resolved to HR using neural networks, and HR observations are assimilated into these HR backgrounds. SRDA methods are computationally efficient because they do not require numerical integration of HR fluid models. Since SRDA has recently been developed, several research questions remain, such as those regarding its theoretical background. For instance, the reasons for combining SR with DA are not clear, apart from the aforementioned reduction in computational costs.

This study proposes a theory of unsupervised SRDA using CVAEs and demonstrates that SR operators can act as background error covariance matrices. This result provides a theoretical foundation for combining SR with DA. We first review an evidence lower bound (ELBO) for DA (Section II), which serves as the loss function for unsupervised learning. We develop a new DA theory using the ELBO and show that this framework is an extension of the traditional 3D-Var method (Section III). This DA theory requires a non-diagonal background error covariance matrix, like the 3D-Var. We then extend the new DA framework by incorporating SR for non-local inference, without estimating such a non-diagonal matrix (Section IV). To evaluate the proposed SRDA, numerical experiments are conducted using an idealized ocean jet system (Section V). The results are analyzed through comparison with an ensemble Kalman filter (Section VI). Conclusions are presented in Section VII. The findings of this study provide a theoretical basis for the fusion of SR and DA, potentially stimulating further research on their integration.

II. FORMULATION OF ELBO FOR DA

We reformulate an evidence lower bound,^{46–48} which is the objective function in the proposed framework. ELBO is also known as the variational lower bound.

The present study considers assimilation at a single time step. In this context, \mathbf{x} , \mathbf{y} , and \mathbf{z} represent a background state, observations, and the true state, respectively, where $\mathbf{x} \in \mathbb{R}^{n_x}$, $\mathbf{y} \in \mathbb{R}^{n_y}$, and $\mathbf{z} \in \mathbb{R}^{n_z}$: \mathbf{x} is a prior forecast from an underlying CFD model, \mathbf{y} represents spatially sparse observations, and \mathbf{z} is the true state vector in the physical space. The objective of DA is to infer \mathbf{z} from \mathbf{x} and \mathbf{y} .

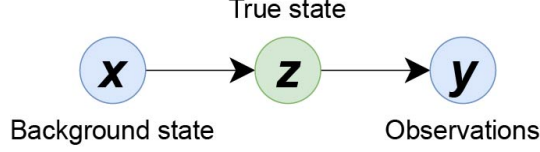


FIG. 1. Probabilistic model expressed by Eq. (1). All variables are in the physical space.

Consider the probabilistic model illustrated in Fig. 1, which is mathematically expressed as

$$p(\mathbf{y} | \mathbf{x}) = \int p(\mathbf{y} | \mathbf{z}) p(\mathbf{z} | \mathbf{x}) d\mathbf{z}. \quad (1)$$

The probability $p(\mathbf{y} | \mathbf{x})$ is decomposed into $p(\mathbf{y} | \mathbf{z})$ and $p(\mathbf{z} | \mathbf{x})$: the former describes the probability of observing \mathbf{y} when the true state is \mathbf{z} and the latter is the prior distribution for \mathbf{z} given the model forecast \mathbf{x} .

The ELBO is derived^{46–48} by introducing an approximate posterior distribution $q(\mathbf{z} | \mathbf{x}, \mathbf{y})$:

$$\ln p(\mathbf{y} | \mathbf{x}) = \ln \left[\int q(\mathbf{z} | \mathbf{x}, \mathbf{y}) \frac{p(\mathbf{y} | \mathbf{z}) p(\mathbf{z} | \mathbf{x})}{q(\mathbf{z} | \mathbf{x}, \mathbf{y})} d\mathbf{z} \right], \quad (2a)$$

$$\geq \int q(\mathbf{z} | \mathbf{x}, \mathbf{y}) \ln \left[\frac{p(\mathbf{y} | \mathbf{z}) p(\mathbf{z} | \mathbf{x})}{q(\mathbf{z} | \mathbf{x}, \mathbf{y})} \right] d\mathbf{z}, \quad (2b)$$

$$= \underbrace{\mathbb{E}_q[\ln p(\mathbf{y} | \mathbf{z})]}_{\text{reconstruction error}} - \underbrace{\mathbb{E}_q \left[\ln \frac{q(\mathbf{z} | \mathbf{x}, \mathbf{y})}{p(\mathbf{z} | \mathbf{x})} \right]}_{\text{KL divergence}} =: -l, \quad (2c)$$

where \mathbb{E}_q is the expectation operator with respect to $q(\mathbf{z} | \mathbf{x}, \mathbf{y})$. Jensen's inequality is applied in Eq. (2b), where the equality holds only when $q(\mathbf{z} | \mathbf{x}, \mathbf{y}) = p(\mathbf{z} | \mathbf{x}, \mathbf{y})$, that is, when the approximate posterior is equal to the exact posterior. In Eq. (2c), the first term is referred to as the reconstruction error for \mathbf{y} , and the second term is known as the Kullback-Leibler (KL) divergence. The final line gives the ELBO ($= -l$), which is the lower bound for the log-likelihood, $\ln p(\mathbf{y} | \mathbf{x})$.

DA is usually performed by maximum likelihood estimation.^{1,2} Instead of maximizing the log-likelihood [i.e., $\ln p(\mathbf{y} | \mathbf{x})$], the proposed framework maximizes the ELBO, or equivalently minimizes l in Eq. (2c), to obtain $q(\mathbf{z} | \mathbf{x}, \mathbf{y})$. The true state \mathbf{z} is then inferred from \mathbf{x} and \mathbf{y} through $q(\mathbf{z} | \mathbf{x}, \mathbf{y})$.

III. DA USING THE ELBO UNDER GAUSSIANTY

We propose a theory of DA using the ELBO and show that this framework is an extension of the 3D-Var formalism. This result explains the necessity of non-diagonal background error covariance matrices, leading to the introduction of SR in Section IV.

A. Transformation of the ELBO under Gaussianity

The following Gaussian distributions are introduced to transform the ELBO:

$$q(z | \mathbf{x}, \mathbf{y}) = \frac{1}{\sqrt{(2\pi)^{n_z} \det V(\mathbf{x}, \mathbf{y})}} \exp\left(-\frac{1}{2} \|\mathbf{z} - \mathbf{A}(\mathbf{x}, \mathbf{y})\|_{V(\mathbf{x}, \mathbf{y})^{-1}}^2\right), \quad (3a)$$

$$p(z | \mathbf{x}) = \frac{1}{\sqrt{(2\pi)^{n_z} \det B}} \exp\left(-\frac{1}{2} \|\mathbf{z} - \mathbf{x}\|_{B^{-1}}^2\right), \quad (3b)$$

$$p(\mathbf{y} | \mathbf{z}) = \frac{1}{\sqrt{(2\pi)^{n_y} \det R}} \exp\left(-\frac{1}{2} \|\mathbf{y} - \mathbf{H}(\mathbf{z})\|_{R^{-1}}^2\right), \quad (3c)$$

where capital letters (e.g., B) denote matrices and sans-serif letters (e.g., \mathbf{A}) denote nonlinear functions that return vectors. The norm $\|\cdot\|$ represents the Mahalanobis distance: $\|\mathbf{z}\|_{B^{-1}}^2 = \mathbf{z}^T B^{-1} \mathbf{z}$ and $\|\mathbf{z}\|^2 = \mathbf{z}^T \mathbf{z}$, where an identity matrix is used when no subscript is present in norm symbols. In Eq. (3a), we assume that the mean $\mathbf{A}(\mathbf{x}, \mathbf{y})$ is the analysis state vector and the covariance matrix $V(\mathbf{x}, \mathbf{y})$ describes the uncertainty of the analysis. For the prior distribution in Eq. (3b), \mathbf{x} and \mathbf{z} belong to the same vector space (i.e., $n_x = n_z$); this assumption is typical for state-space models.⁴⁹ The observation operator \mathbf{H} in Eq. (3c) converts the true state into the observation space. The prescribed background- and observation-error covariance matrices are denoted by B and R , respectively.

The ELBO is transformed by substituting Eqs. (3a)–(3c) into (2c). The first term, the reconstruction error in Eq. (2c), becomes

$$\mathbb{E}_q[\ln p(\mathbf{y} | \mathbf{z})] = \mathbb{E}_q\left[-\frac{1}{2} \|\mathbf{y} - \mathbf{H}(\mathbf{z})\|_{R^{-1}}^2 - \frac{n_y}{2} \ln(2\pi) - \frac{1}{2} \ln(\det R)\right], \quad (4a)$$

$$\approx -\frac{1}{n_{\text{sample}}} \frac{1}{2} \sum_{\text{sample}} \|\mathbf{y} - \mathbf{H}(\hat{\mathbf{z}})\|_{R^{-1}}^2 + \text{const}, \quad (4b)$$

where

$$\hat{\mathbf{z}} = \mathbf{A}(\mathbf{x}, \mathbf{y}) + \boldsymbol{\varepsilon}^T V(\mathbf{x}, \mathbf{y})^{1/2} = \mathbf{a} + \boldsymbol{\varepsilon}^T V^{1/2}. \quad (5)$$

Here, the expected value is approximated by the sample mean using a Monte Carlo method (i.e., the reparameterization trick⁹). In the actual implementation, the sample size n_{sample} can be set to 1 if the batch size is sufficiently large.⁹ Each realization $\hat{\mathbf{z}}$ is sampled from $q(z | \mathbf{x}, \mathbf{y})$, where \mathbf{a} and V denote the vector and the matrix given by $\mathbf{A}(\mathbf{x}, \mathbf{y})$ and $V(\mathbf{x}, \mathbf{y})$, respectively, $\boldsymbol{\varepsilon}$ is an n_z -dimensional standard normal variable, and $V^{1/2}$ is obtained by Cholesky decomposition. Equation (4b) indicates that the reconstruction error measures the difference between \mathbf{y} and $\mathbf{H}(\hat{\mathbf{z}})$ in the observation space.

The KL divergence, the second term in Eq. (2c), is transformed as follows:

$$\mathbb{E}_q \left[\ln \frac{q(\mathbf{z} | \mathbf{x}, \mathbf{y})}{p(\mathbf{z} | \mathbf{x})} \right] = \int d\mathbf{z} q(\mathbf{z} | \mathbf{x}, \mathbf{y}) \left\{ -\frac{1}{2} \ln [\det V(\mathbf{x}, \mathbf{y})] - \frac{1}{2} \|\mathbf{z} - \mathbf{A}(\mathbf{x}, \mathbf{y})\|_{V(\mathbf{x}, \mathbf{y})^{-1}}^2 \right\},$$

$$- \int d\mathbf{z} q(\mathbf{z} | \mathbf{x}, \mathbf{y}) \left\{ -\frac{1}{2} \ln [\det B] - \frac{1}{2} \|\mathbf{z} - \mathbf{x}\|_{B^{-1}}^2 \right\}, \quad (6a)$$

$$= \frac{1}{\sqrt{(2\pi)^{n_z}}} \int d\tilde{\mathbf{z}} \exp \left(-\frac{\|\tilde{\mathbf{z}}\|^2}{2} \right) \left\{ -\frac{1}{2} \ln \left[\frac{\det V(\mathbf{x}, \mathbf{y})}{\det B} \right] \right.$$

$$\left. + \frac{1}{2} \left\| \left[\tilde{\mathbf{z}}^T V(\mathbf{x}, \mathbf{y})^{1/2} + \mathbf{A}(\mathbf{x}, \mathbf{y}) \right] - \mathbf{x} \right\|_{B^{-1}}^2 \right\} + \text{const}, \quad (6b)$$

$$= \frac{1}{2} \|\mathbf{A}(\mathbf{x}, \mathbf{y}) - \mathbf{x}\|_{B^{-1}}^2 + \frac{1}{2} \left\{ \text{tr} [B^{-1} V(\mathbf{x}, \mathbf{y})] - \ln \left[\frac{\det V(\mathbf{x}, \mathbf{y})}{\det B} \right] \right\} + \text{const} \quad (6c)$$

To perform the integral, we use an auxiliary variable $\tilde{\mathbf{z}} = V(\mathbf{x}, \mathbf{y})^{-1/2} [\mathbf{z} - \mathbf{A}(\mathbf{x}, \mathbf{y})]$. The first term in Eq. (6c) represents the difference between the analysis $\mathbf{A}(\mathbf{x}, \mathbf{y})$ and the background state \mathbf{x} , while the second term is a convex function of $V(\mathbf{x}, \mathbf{y})$, which takes the minimum when $V(\mathbf{x}, \mathbf{y}) = B$.

Using Eqs. (4b) and (6c), the ELBO in Eq. (2c) is transformed into

$$l_{\text{Gauss}} = \frac{1}{2} \|\mathbf{y} - \mathbf{H}(\hat{\mathbf{z}})\|_{R^{-1}}^2 + \frac{1}{2} \|\mathbf{A}(\mathbf{x}, \mathbf{y}) - \mathbf{x}\|_{B^{-1}}^2 + \frac{1}{2} \left\{ \text{tr} [B^{-1} V(\mathbf{x}, \mathbf{y})] - \ln \left[\frac{\det V(\mathbf{x}, \mathbf{y})}{\det B} \right] \right\}, \quad (7)$$

where constant terms are omitted and the sample size is set to 1 in Eq. (4b).

B. Reduction of the ELBO to the 3D-Var objective function

We show that l_{Gauss} in Eq. (7) can be reduced to the 3D-Var objective function. This result suggests that DA can be performed by minimizing l_{Gauss} .

To show this result, we set the covariance $V(\mathbf{x}, \mathbf{y})$ to a constant and quite small matrix. In this case, $\hat{\mathbf{z}}$ in Eq. (5) becomes $\hat{\mathbf{z}} = \mathbf{A}(\mathbf{x}, \mathbf{y}) = \mathbf{a}$ and the third term in Eq. (7) becomes constant. Therefore, l_{Gauss} is reduced to $l_{\text{3D-Var}}$:

$$l_{\text{3D-Var}} = \frac{1}{2} \|\mathbf{y} - \mathbf{H}(\mathbf{a})\|_{R^{-1}}^2 + \frac{1}{2} \|\mathbf{a} - \mathbf{x}\|_{B^{-1}}^2, \quad (8)$$

where \mathbf{a} denotes the analysis vector given by the function \mathbf{A} from the inputs \mathbf{x} and \mathbf{y} . The function $l_{\text{3D-Var}}$ is equivalent to the 3D-Var objective function,^{1,2,24} and the vector \mathbf{a} is obtained by minimizing $l_{\text{3D-Var}}$. The first term of $l_{\text{3D-Var}}$, which comes from the reconstruction error in Eq. (2c), compares the observation vector \mathbf{y} and the analysis \mathbf{a} through the observation operator \mathbf{H} . The

second term of l_{3D-Var} , which comes from the KL divergence in Eq. (2c), measures the difference between the analysis \mathbf{a} and the background state \mathbf{x} . By minimizing l_{3D-Var} , \mathbf{y} and \mathbf{x} are integrated, and the true state is estimated as \mathbf{a} . These results suggest that the ELBO describes the balance between observations and background states in estimating the true state.

The minimizer of l_{3D-Var} is easily derived when the observation operator is linear (i.e., $H = H$, where H is a matrix).^{1,2}

$$\mathbf{a} = \mathbf{x} + K(\mathbf{y} - H\mathbf{x}), \quad (9a)$$

$$K = BH^T(R + HBH^T)^{-1}, \quad (9b)$$

where K is known as the Kalman gain matrix. The second term in Eq. (9a) describes the non-local nature of DA. The background state \mathbf{x} is corrected through the spatially sparse observations \mathbf{y} by the non-diagonal matrix K . Typically, this non-diagonal property originates from the non-zero off-diagonal elements of the background error covariance matrix B . In other words, the non-local correction is realized through the spatial correlation patterns of background values. The necessity of spatial correlations leads to a difficulty for DA by neural networks (Section III C).

C. Implementation of DA by CVAE

DA can be performed by solving the minimization problem of l_{Gauss} . However, this minimization at every assimilation time step would be computationally intensive. We propose to efficiently conduct this minimization using a trained CVAE.

Generally, the loss function for VAEs, including CVAEs, is an ELBO.^{7,9,10,12,13} This can be understood from the ELBO formula, Eq. (7). To evaluate l_{Gauss} , the analysis \mathbf{a} and its covariance V are first computed from a given input of \mathbf{x} and \mathbf{y} ; then, the observation vector $\hat{\mathbf{y}} (= H(\hat{\mathbf{z}}))$ is reconstructed from \mathbf{a} and V via Eq. (5). The value of l_{Gauss} decreases as $\hat{\mathbf{y}}$ becomes closer to the input \mathbf{y} . The structure that reconstructs the input is common to autoencoders.¹¹ The second and third terms in Eq. (7) are considered as the conditions for the estimated true state $\hat{\mathbf{z}}$. For instance, l_{Gauss} is decreased as \mathbf{a} becomes close to \mathbf{x} . Thus, a CVAE is necessary to incorporate these conditions, and this CVAE is trained by minimizing l_{Gauss} .

The CVAE consists of an encoder and a decoder (Fig. 2). The encoder estimates \mathbf{a} and V from the input \mathbf{x} and \mathbf{y} , while the decoder reconstructs $\hat{\mathbf{y}}$. In other words, the encoder performs assimilation and the decoder acts as the nonlinear observation operator. The encoder learns how

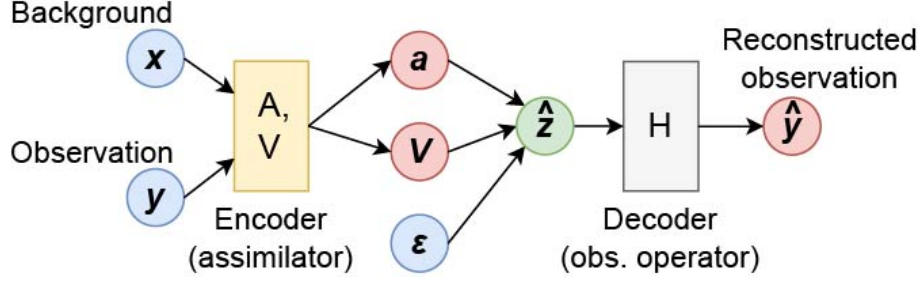


FIG. 2. Architecture of the CVAE for DA. The encoder estimates the analysis vector \mathbf{a} and its covariance V , both of which give a sample of the true state $\hat{\mathbf{z}}$ in Eq. (5). The decoder acts as the observation operator and reconstructs the observation vector $\hat{\mathbf{y}} = H(\hat{\mathbf{z}})$.

to integrate \mathbf{x} and \mathbf{y} , yielding the analysis \mathbf{a} , while the decoder learns how to convert \mathbf{a} into the observation space. Once the CVAE is trained, the encoder performs DA without minimizing l_{Gauss} as long as the statistics of the background \mathbf{x} and the observations \mathbf{y} do not change significantly.

The covariance matrices R and B in l_{Gauss} are treated as prescribed parameters (i.e., hyperparameters). Since it is difficult to determine many hyperparameters, these matrices are usually assumed to be proportional to identity matrices: $R = rI_{n_y}$ and $B = bI_{n_z}$, where I_n is an identity matrix of size n , and r and b are positive real parameters. However, off-diagonal elements of B describe the spatial correlation patterns of background states and are essential for the non-local estimation in DA (Section III B).

There are several methods for implementing non-local estimation. For instance, latent variables can be transformed to have covariance or even follow non-Gaussian distributions by combining VAEs and normalizing flows,^{50,51} where this transformation is learnable from data. An alternative approach is to divide observed values used as input to CVAEs and those targeted for reconstruction. CVAEs reconstruct observations from the other observations at different grid points, which enables CVAEs to learn non-locality. A similar technique is employed in MetNet-3, a surrogate neural network for weather predictions developed by Google.⁵² As a final method, we adopt super-resolution (SR). The non-locality is incorporated into CVAEs through SR even when B and R are diagonal.

IV. SRDA USING THE ELBO

We incorporate SR into the DA theory proposed in Section III. A key characteristic of SR models is their non-locality:^{37,38} SR models map LR patterns with a certain spatial extent to HR patterns. These SR mappings (i.e., SR operators) are integrated into DA, resulting in SRDA, which facilitates the non-local correction of background values by observations across distant grid points.

A. Integration of SR into DA

To develop a theory of SRDA, we specify the resolutions of a background state \mathbf{x} , observations \mathbf{y} , and the true state \mathbf{z} : \mathbf{x} is defined at LR grid points, while \mathbf{y} and \mathbf{z} are defined at HR grid points. The vector forms are obtained by arranging three-dimensional grid point values into columns. Observations are not available at all locations due to various factors, such as measurement errors. These missing grid points are excluded when arranging observations into the column vector \mathbf{y} .

We modify the probability distributions in Eqs. (3a)–(3c) for SRDA:

$$q(\mathbf{z} | \mathbf{x}, \mathbf{y}) = \frac{1}{\sqrt{(2\pi)^{n_z} \det V(\mathbf{x}, \mathbf{y})}} \exp \left\{ -\frac{1}{2} \|\mathbf{z} - \mathbf{A}_{\text{HR}}(\mathbf{x}, \mathbf{y})\|_{V(\mathbf{x}, \mathbf{y})}^2 \right\}, \quad (10a)$$

$$p(\mathbf{z} | \mathbf{x}) = \frac{1}{(\sqrt{2\pi b})^{n_z}} \exp \left\{ -\frac{1}{2b} \|\mathbf{z} - \mathbf{F}(\mathbf{x})\|^2 \right\}, \quad (10b)$$

$$p(\mathbf{y} | \mathbf{z}) = \frac{1}{(\sqrt{2\pi r})^{n_y}} \exp \left\{ -\frac{1}{2r} \|\mathbf{y} - \mathbf{H}(\mathbf{z})\|^2 \right\}, \quad (10c)$$

where

$$\mathbf{A}_{\text{HR}} = \mathbf{F} \circ \mathbf{A}_{\text{LR}}. \quad (11)$$

We first explain the differences between Eqs. (3) and (10) due to B and R being diagonal. The covariance matrices are $B = bI_{n_z}$ and $R = rI_{n_y}$, where b and r are prescribed positive real numbers and I_n is an identity matrix of size n . The exponents are then expressed as $\|\mathbf{z} - \mathbf{F}(\mathbf{x})\|_{B}^2 = \|\mathbf{z} - \mathbf{F}(\mathbf{x})\|^2 / b$ and $\|\mathbf{y} - \mathbf{H}(\mathbf{z})\|_{R}^2 = \|\mathbf{y} - \mathbf{H}(\mathbf{z})\|^2 / r$ in Eqs. (10b) and (10c), respectively. Note that the norm $\|\cdot\|$ with no subscript uses an identity matrix, such as $\|\mathbf{z}\|^2 = \mathbf{z}^T I_{n_z} \mathbf{z} = \mathbf{z}^T \mathbf{z}$. The determinants are expressed as $\det B = b^{n_z}$ and $\det R = r^{n_y}$. We also take the covariance $V(\mathbf{x}, \mathbf{y})$ in Eq. (10a) to be diagonal:

$$V(\mathbf{x}, \mathbf{y}) = \text{diag} [v_1(\mathbf{x}, \mathbf{y}), \dots, v_{n_z}(\mathbf{x}, \mathbf{y})], \quad (12)$$

where each variance $v_i(\mathbf{x}, \mathbf{y})$ ($i = 1, \dots, n_z$) is a positive value determined by the vectors \mathbf{x} and \mathbf{y} .

There are two essential changes from Eqs. (3) to (10). First, an SR operator F is introduced in Eq. (10b), where F maps an n_x -dimensional vector into an n_z -dimensional vector. Since \mathbf{x} and \mathbf{z} are defined at LR and HR grid points, respectively (i.e., $n_x < n_z$), this mapping performs SR. Comparing Eqs. (3b) and (10b), the mean of the prior distribution $p(\mathbf{z} | \mathbf{x})$ is replaced with the super-resolved background state $F(\mathbf{x})$. Second, the analysis state is also super-resolved using F . The function A in Eq. (3a) is replaced with a composition $A_{\text{HR}} = F \circ A_{\text{LR}}$ in Eq. (10a): the LR analysis is first calculated as $\mathbf{a}_{\text{LR}} = A_{\text{LR}}(\mathbf{x}, \mathbf{y})$ and then it is super-resolved as $\mathbf{a}_{\text{HR}} = F(\mathbf{a}_{\text{LR}})$. The influences of these two changes are further discussed in Sections IV B and IV C.

The ELBO is transformed by substituting Eqs. (10a)–(10c) into (2c), as in Section III A:

$$l_{\text{SRDA}} = \frac{1}{2r} \|\mathbf{y} - H(\hat{\mathbf{z}})\|^2 + \frac{1}{2b} \|A_{\text{HR}}(\mathbf{x}, \mathbf{y}) - F(\mathbf{x})\|^2 + \frac{1}{2} \sum_{i=1}^{n_z} \left\{ \frac{v_i(\mathbf{x}, \mathbf{y})}{b} - \ln \left[\frac{v_i(\mathbf{x}, \mathbf{y})}{b} \right] \right\}, \quad (13)$$

where

$$\mathbf{a}_{\text{HR}} = A_{\text{HR}}(\mathbf{x}, \mathbf{y}) = F(A_{\text{LR}}(\mathbf{x}, \mathbf{y})), \quad (14a)$$

$$\mathbf{a}_{\text{LR}} = A_{\text{LR}}(\mathbf{x}, \mathbf{y}), \quad (14b)$$

$$\hat{\mathbf{z}} = A_{\text{HR}}(\mathbf{x}, \mathbf{y}) + \varepsilon^T V(\mathbf{x}, \mathbf{y})^{1/2} = F(\mathbf{a}_{\text{LR}}) + \sum_{i=1}^{n_z} \varepsilon_i \sqrt{v_i}. \quad (14c)$$

Eqs. (13) and (14c) corresponds to Eqs. (7) and (5) in Section III A, respectively. Like in Eq. (7), the Monte Carlo method (i.e., the reparameterization trick⁹) is applied in Eq. (13) with the sample size being 1. In the right-hand side of Eq. (14c), the arguments of \mathbf{x} and \mathbf{y} are omitted, and the definitions of \mathbf{a}_{HR} and \mathbf{a}_{LR} are used. The first term of l_{SRDA} represents the difference between the observation vector \mathbf{y} and the estimated true state $H(\hat{\mathbf{z}})$ in the observation space. The second term is the difference between the super-resolved analysis $F(\mathbf{a}_{\text{LR}})$ and the super-resolved background $F(\mathbf{x})$. The third term is a convex function of v_i , which takes the minimum when $v_i(\mathbf{x}, \mathbf{y}) = b$. These points indicate that the ELBO describes the balance between the observations and the super-resolved forecast in estimating the HR true state.

B. Case of linear SR

We interpret l_{SRDA} in Eq. (13) using a linear SR operator and show that SR operators act as background error covariance matrices. Linear SR operators were frequently used in SR studies, especially in theoretical studies, before the emergence of deep learning.⁵³ When generation processes of LR images from HR images are linear (e.g., subsampling and blurring), the inverse

processes, namely the SR processes, are also linear.⁵³ Here, an SR operator is denoted as a matrix F , which has the size of $n_z \times n_x$ ($n_z > n_x$) and maps n_x -dimensional LR vectors into n_z -dimensional HR vectors. Since SR is generally non-local, the matrix F has non-zero off-diagonal elements.

To simplify the discussion, we take the variances v_i ($i = 1, \dots, n_z$) to be constant and small values, as in Section III B. The estimated true state \hat{z} in Eq. (14c) is then equal to $\hat{z} = F\mathbf{a}_{\text{LR}}$. Further, the third term in Eq. (13) is ignored because it becomes constant.

Thus, l_{SRDA} is reduced to

$$l_{\text{linear SRDA}} = \frac{1}{2r} \|\mathbf{y} - \mathbf{H}(F\mathbf{a}_{\text{LR}})\|^2 + \frac{1}{2b} (\mathbf{a}_{\text{LR}} - \mathbf{x})^T (F^T F) (\mathbf{a}_{\text{LR}} - \mathbf{x}). \quad (15)$$

The matrix $F^T F$ is an $n_x \times n_x$ positive semi-definite matrix. Compared to the ELBO for 3D-Var in Eq. (8), $F^T F$ can be interpreted as the covariance matrix B and describes the spatial correlations among the LR components.

When the observation operator is linear ($\mathbf{H} = H$) as in Section III B, the minimizer for $l_{\text{linear SRDA}}$ is always obtained due to the convexity of $l_{\text{linear SRDA}}$. We first consider the case where $F^T F$ is positive definite (i.e., invertible). The minimizer is then derived, as in Eq. (9):

$$\mathbf{a}_{\text{LR}} = \mathbf{x} + \tilde{K} (\mathbf{y} - \tilde{H}\mathbf{x}), \quad (16a)$$

$$\tilde{K} = \tilde{B}\tilde{H}^T (rI_{n_y} + \tilde{H}\tilde{B}\tilde{H}^T)^{-1}, \quad (16b)$$

where $\tilde{B} = b(F^T F)^{-1}$ and $\tilde{H} = HF$. The observation operator for the LR background is given by $\tilde{H} = HF$ through the SR operator F . Generally, the Kalman gain matrix \tilde{K} has non-zero off-diagonal elements due to F being non-diagonal. Thus, the LR background \mathbf{x} is non-locally corrected by the observations \mathbf{y} , giving the LR analysis \mathbf{a}_{LR} in Eq. (16a).

Even when $F^T F$ is positive semi-definite (i.e., at least one eigenvalue is zero), minimizers for $l_{\text{linear SRDA}}$ exist due to its convexity. In this case, a solution similar to Eq. (16a) is derived using pseudo-inverse matrices (not shown in detail).

C. Case of non-linear SR

In practice, SR models are neural networks, so SR operators are non-linear. Since the nonlinear case includes the linear case, the non-local inference is achieved in both cases. Here, we briefly examine non-linear SR operators from a different perspective: the transformation of probability distributions.

We consider a complete non-linear SR operator F , that is, a bijective SR operator. Rigorously speaking, SR is an inverse problem and SR operations are not bijective; however, a virtual bijective map is sometimes considered in theoretical studies of SR. In this case, any HR true state z has the corresponding LR state: $z_{\text{LR}} = F^{-1}(z)$ and $z = F(z_{\text{LR}})$. We can regard the posterior and prior distributions in Eqs. (10a) and (10b) as non-Gaussian distributions for z_{LR} :

$$q(z_{\text{LR}} | \mathbf{x}, \mathbf{y}) = \frac{|DF|}{\sqrt{(2\pi)^{n_z} \det V(\mathbf{x}, \mathbf{y})}} \exp \left\{ -\frac{1}{2} \|\mathbf{F}(z_{\text{LR}}) - \mathbf{F}(\mathbf{A}_{\text{LR}}(\mathbf{x}, \mathbf{y}))\|_{V(\mathbf{x}, \mathbf{y})^{-1}}^2 \right\}, \quad (17a)$$

$$p(z_{\text{LR}} | \mathbf{x}) = \frac{|DF|}{(\sqrt{2\pi b})^{n_z}} \exp \left\{ -\frac{1}{2b} \|\mathbf{F}(z_{\text{LR}}) - \mathbf{F}(\mathbf{x})\|^2 \right\}, \quad (17b)$$

where $|DF|$ denotes the Jacobian determinant of F .

This result suggests that SR operators can be interpreted as normalizing flows.^{50,51} Normalizing flow is a deep generative model that converts Gaussian variables into non-Gaussian variables, generating new data that obey complicated probability distributions. In normalizing flows, invertible non-linear transformations are implemented as neural-network layers and are stacked to form the whole network to achieve complex transformations. Importantly, normalizing flows can be used to transform latent variables in VAEs.^{50,51} This combined architecture is similar to the CVAE proposed in the present study (Section IV E), where the SR model transforms \mathbf{a}_{LR} into \mathbf{a}_{HR} inside the encoder. This similarity implies the potential for using normalizing flows to further develop SRDA.

D. Loss function for SR models

So far, we have employed the SR operator F , namely the trained SR model. This section presents a loss function for training this model. We do not know the true state of the system and only know the LR background \mathbf{x} and the HR observations \mathbf{y} . The former \mathbf{x} is spatially complete, while the latter \mathbf{y} is spatially incomplete. The SR model is trained in this setup.

We propose the following loss function to train SR models:

$$l_{\text{SR}} = \sum_{i=1}^{n_y} |y_i - [PF(\mathbf{x})]_i|, \quad (18)$$

where $|\cdot|$ denotes the absolute value, i specifies vector components, and P is the projection matrix into the observation space. The right-hand side clarifies that l_{SR} is an L1 norm, which is frequently used in SR studies.^{25,26,36} Since l_{SR} is differentiable with respect to $F(\mathbf{x})$, backpropagation can be

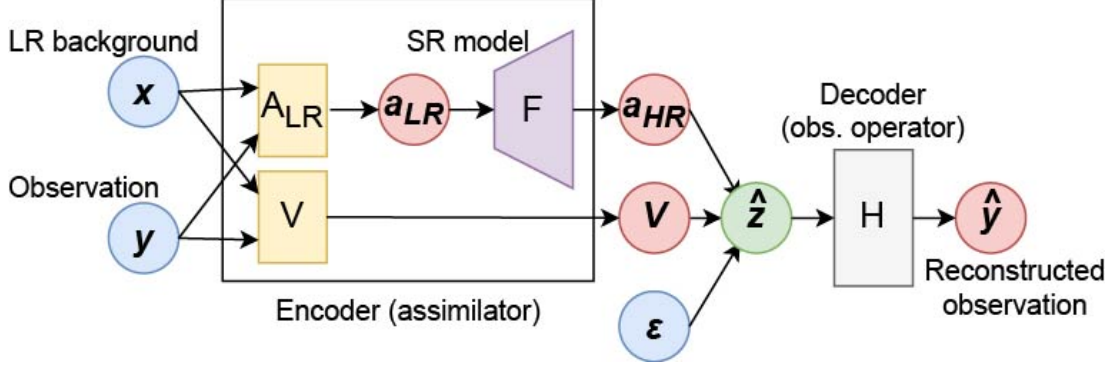


FIG. 3. Architecture of the CVAE for SRDA. The encoder estimates the HR analysis vector \mathbf{a}_{HR} using the SR model. The encoder also estimates the covariance V for \mathbf{a}_{HR} . The variables \mathbf{a}_{HR} and V give a sample of the true state $\hat{\mathbf{z}}$ in Eq. (14c). The decoder acts as the observation operator and reconstructs the observation vector $\hat{\mathbf{y}} = H(\hat{\mathbf{z}})$.

performed; that is, the SR model F can be trained in a supervised manner, where the input is \mathbf{x} and the target is \mathbf{y} . When the training data size is sufficiently large, the trained SR model infers the median of \mathbf{y} conditioned on \mathbf{x} , as shown in Hastie et al.⁵⁴ This fact suggests that the SR model can make unbiased inferences if the median of the observation error distribution is zero.

E. Implementation of SRDA by CVAE

The efficient minimization of l_{SRDA} in Eq. (13) is possible with CVAEs, similar to Section III C. Thus, SRDA can be implemented using CVAEs.

The CVAE for SRDA consists of an encoder and a decoder (Fig. 3). The difference from the CVAE in Fig. 2 is that the encoder incorporates an SR model and performs SR and DA simultaneously. Here, we employ the SR model described in Section IV D, which is trained with the loss function in Eq. (18). This encoder integrates the LR background \mathbf{x} and the HR observations \mathbf{y} and estimates the HR analysis \mathbf{a}_{HR} through computing the LR analysis \mathbf{a}_{LR} . The encoder also estimates the uncertainty of \mathbf{a}_{HR} by calculating the variances. The decoder acts as the observation operator, as in Fig. 2. The CVAE is trained in an unsupervised manner using l_{SRDA} as the loss function.

Strictly speaking, a different SR model should be used within the encoder because the SR model in Section IV D is trained to super-resolve the LR background \mathbf{x} , which differs from the LR analysis \mathbf{a}_{LR} . This difference in input may introduce bias to \mathbf{a}_{LR} . In other words, the trained SR

model assumes \boldsymbol{x} as input and may lead to a bias of $\boldsymbol{a}_{\text{LR}}$ similar to that of \boldsymbol{x} . On the other hand, the output $\boldsymbol{a}_{\text{HR}} (= F(\boldsymbol{a}_{\text{LR}}))$ is expected to be less biased because the SR-model output is unbiased if the observation error distribution has a zero median (Section IV D). Thus, $\boldsymbol{a}_{\text{HR}}$ is used as the initial conditions for LR fluid models by resizing $\boldsymbol{a}_{\text{HR}}$ to the LR (Section IV F). One solution for making $\boldsymbol{a}_{\text{LR}}$ less biased is to conduct fine-tuning of the SR model during the training of the CVAE. For simplicity, however, the present study does not use such an advanced learning method, which remains a future research topic.

F. Sequential SRDA by the CVAE

We introduce a sequential SRDA method applicable to CFD simulations. The background state \boldsymbol{x} is hereafter referred to as the forecast state because it is a prior forecast given by an LR fluid model. The forecast and assimilation are executed alternately, as in other statistical DA methods,^{1,2} such as 3D-Var. This assimilation is performed using a trained CVAE’s encoder (Fig. 3).

Figure 4 shows a schematic of the sequential SRDA. Here, we assume a constant assimilation interval ΔT . At every assimilation time step, the encoder assimilates the HR observations \boldsymbol{y} into the LR forecast state \boldsymbol{x} , thereby estimating the HR analysis $\boldsymbol{a}_{\text{HR}}$. This output is resized to the LR using an algebraic method, such as linear interpolation. In the next assimilation cycle, the resized analysis is used as the initial condition for the LR fluid model, and forecasts are computed by numerical integration over ΔT . The forecast at the final time step is fed to the encoder to infer the subsequent HR analysis.

The decoder is not used in the sequential SRDA; rather, it is used only in the training phase to learn the observation operator (Section IV E). In contrast, the trained SR model can be used in the test phase (i.e., the operational phase) to super-resolve LR forecast states. This SR operation is independent of assimilation, allowing for the generation of HR forecast states at any time step (Section VI C).

V. METHODS

We evaluate the proposed SRDA method through numerical experiments similar to observing-system simulation experiments (OSSEs).⁵⁵ The ground truth (or the nature run) is generated by an HR fluid model, from which pseudo (or synthetic) observations are computed. The SRDA

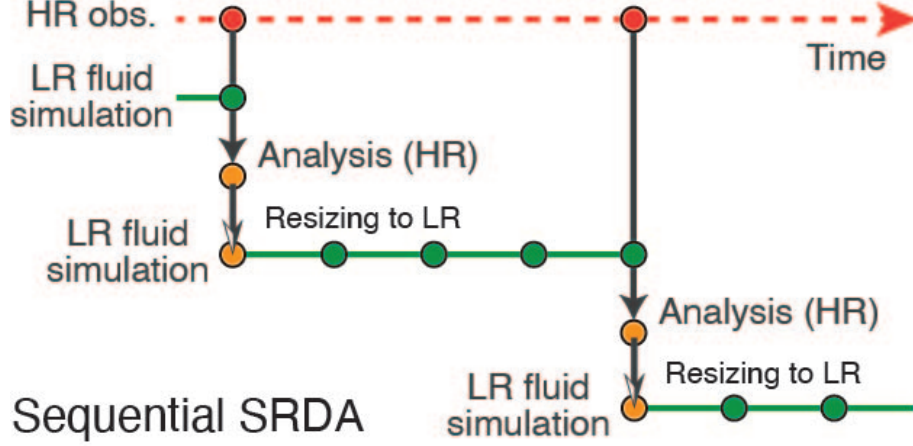


FIG. 4. Schematic of the sequential SRDA. “HR obs” denotes HR observations. A constant assimilation interval ΔT is assumed, where the output time step is a quarter of ΔT as an example.

employs an LR version of the fluid model, and the resultant forecast and analysis are compared with the ground truth. A simple jet stream system was adopted for these experiments, as a proof of concept for the SRDA.

A. Fluid simulation

An idealized barotropic ocean jet, proposed by David et al.,⁵⁶ was simulated in a two-dimensional periodic channel, using the same configuration as in Yasuda and Onishi.⁴⁰ The experimental setup is briefly explained here. See the above references for further details.

The governing equations in the periodic channel (x, y) are as follows⁵⁶

$$\frac{\partial \omega}{\partial t} + \mathbf{u} \cdot \nabla \omega + \beta \frac{\partial \psi}{\partial x} = -\kappa \omega - \nu \Delta^2 \omega - \frac{d\tau(y)}{dy}, \quad (19a)$$

$$\Delta \psi = \omega, \quad (19b)$$

$$\mathbf{u} = \left(-\frac{\partial \psi}{\partial y}, \frac{\partial \psi}{\partial x} \right), \quad (19c)$$

where x is the channel-wise direction and y is the transverse direction ($x \in [0, 2\pi]$ and $y \in [0, \pi]$). Equation (19a) describes the evolution of vorticity ω over time t . The left-hand side represents the advection of ω and the beta effect,⁵⁷ while the right-hand side comprises linear drag, hyperviscosity, and forcing due to zonal wind stress $\tau(y)$. Equations (19b) and (19c) define the stream function ψ and the velocity \mathbf{u} , respectively.

The parameters in Eq. (19a) were set as follows: $\beta = 0.1$, $\kappa = 1 \times 10^{-2}$, and $\nu = 1 \times 10^{-5}$.

TABLE I. Fluid simulation configurations at two different spatial resolutions: LR and HR. The cutoff wavenumber is the maximum wavenumber magnitude in the CFD model, which was determined by the specific condition to avoid aliasing errors in the pseudo-spectral method (i.e., the 2/3-rule).⁵⁹

Name	Grid size ($x \times y$)	Cutoff wavenumber	Integration time step
LR (low resolution)	32×16	10	5×10^{-4}
HR (high resolution)	128×64	42	$\frac{1}{4} \times 5 \times 10^{-4}$

The wind stress was given by

$$\tau(y) = \tau_0 \left[\operatorname{sech}^2 \left(\frac{y - y_0}{\delta} \right) - c \right], \quad (20)$$

where $\tau_0 = 0.3$, $y_0 = \pi/2$, $\delta = 0.4$, and c was adjusted such that the integral of $\tau(y)$ was zero. This setup falls within the parameter regime of mixing barriers with strong eddies,⁵⁶ where coherent vortices persist in a statistically steady state (Section VI A).

The initial condition was a zonal jet superimposed with random perturbations. The zonal jet adopts the same shape as $\tau(y)$ and satisfies the Rayleigh-Kuo inflection-point criterion,⁵⁸ which is a necessary condition for barotropic instability. Perturbations were added to the vorticity field for each wavenumber component, with phase and amplitude drawn from Gaussian distributions. The simulation data for deep learning were generated by varying these random perturbations.

Numerical integration was conducted using the modified Euler and pseudo-spectral methods at two spatial resolutions: LR and HR. Table I provides detailed configurations for the LR and HR. All simulations ran from $t = 0$ to 20 with output time intervals of 0.25. The CFD models using the LR and HR configurations are referred to as the LR and HR fluid models, respectively.

B. Synthetic observations

Synthetic observations were generated from the HR simulations. We consider an idealized point-wise observation network that imitates moored buoys in the ocean or balloon-borne radiosondes in the atmosphere.^{60,61} Observed grid points were randomly subsampled at constant spatial intervals, namely 8×8 grids, which means that 1.56% ($= 1/8^2$) of grid points are observed. To demonstrate that the SRDA can address changes in observed points, the subsampled points were varied in time by random shifts. For the unobserved points, Not a Numbers (NaNs) were assigned and replaced with missing values in the subsequent preprocessing (Section V C). To

emulate measurement errors, spatially independent Gaussian noise was added to the subsampled vorticity. The noise has a mean of 0 and a standard deviation of 0.1. This standard deviation is approximately 5% of the spatio-temporal average of the absolute values of vorticity.

C. Neural networks

We outline the network architectures of an SR model and a CVAE for the sequential SRDA (Section IV F). Hyperparameters are provided in Appendix and the full implementation is available at our GitHub repository (see Data Availability Statement). PyTorch 1.11.0⁶² was used for the implementation.

The SR model architecture is shown by the top panel in Fig. 5. This model resembles the neural network for SR known as VDSR, proposed by Kim et al.⁶³ The input is the two-dimensional vorticity field obtained from the LR fluid model, namely the LR forecast state, which is super-resolved to the HR. First, this input is nonlinearly transformed through a stack of convolution and ReLU layers. Upsampling is then executed by two blocks that include pixel shuffle layers.⁶⁴ Each block doubles the size of each dimension, resulting in a fourfold increase in resolution. Additionally, a skip connection⁶⁵ is employed, whereby the LR input, resized by bicubic interpolation, is added to the final output. This skip connection allows the SR model to capture small-scale patterns, that is, discrepancies between the LR input and the HR output.

The CVAE consists of an encoder and a decoder (Fig. 5). The encoder performs SRDA and integrates the inputs, an LR forecast and an HR observation, into the HR analysis. The HR observation is first downsampled through convolution to align the resolution to the LR (totally, downsampled by a factor of 4). The LR forecast and the downsampled observation are then concatenated and passed through residual blocks to obtain the LR analysis \mathbf{a}_{LR} . Then, \mathbf{a}_{LR} is super-resolved by the trained SR model to the HR analysis \mathbf{a}_{HR} . The variance for \mathbf{a}_{HR} is denoted as V in Eq. (12) and is also estimated by the encoder. Although V and \mathbf{a}_{HR} can be treated independently in the encoder (Section IV E), the present study computes V from \mathbf{a}_{LR} to reduce the number of neural network parameters. Moreover, we employed the feature extractor in the trained SR model to compute V (Feature Extractor-1 in Fig. 5).

The decoder acts as an observation operator and reconstructs the observations from \hat{z} . This operation is achieved through a stack of convolutional and Leaky ReLU⁶⁶ layers. We confirmed that the decoder can be replaced with a subsampling operation (not a neural network), although

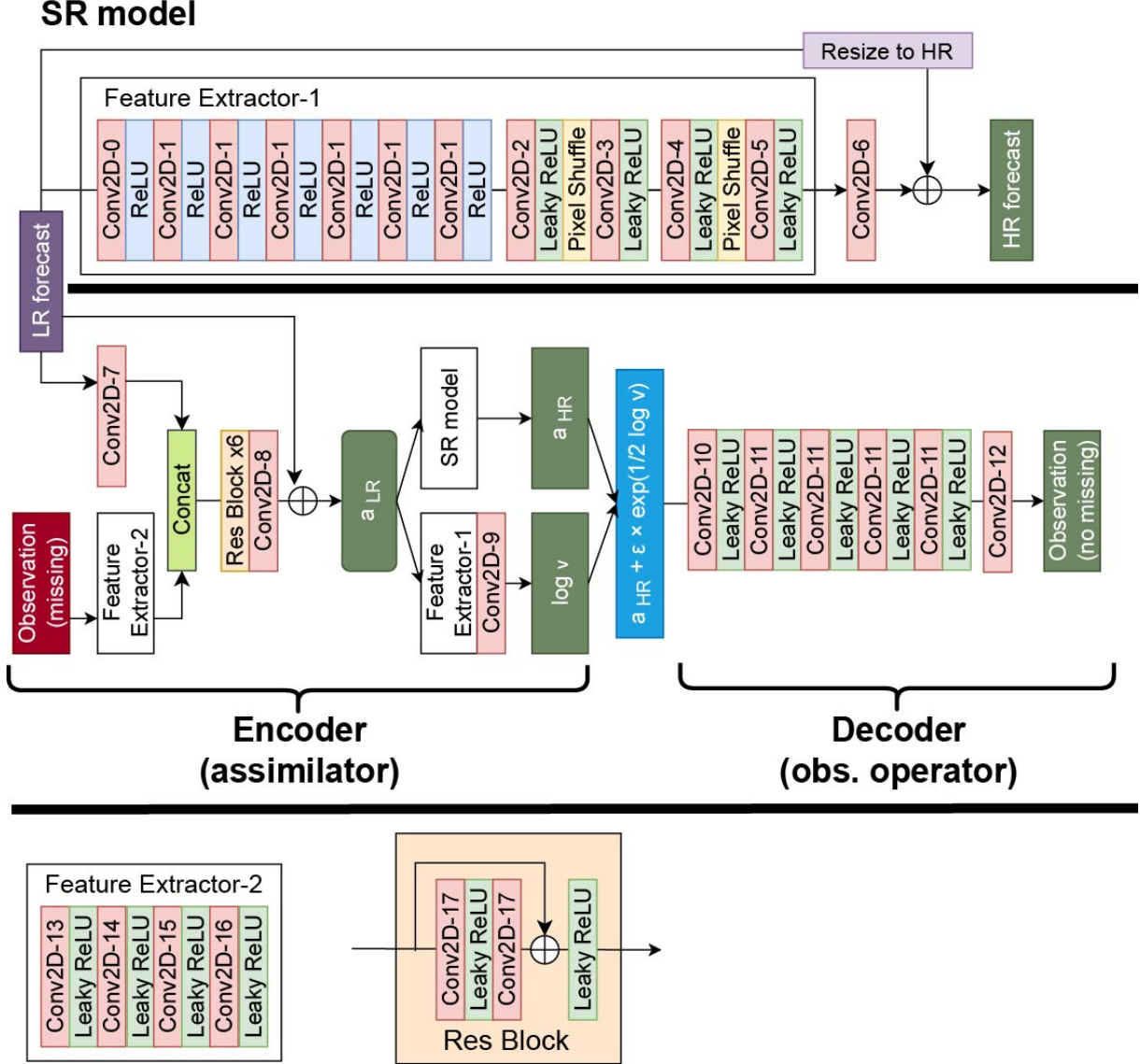


FIG. 5. Network architectures of the SR model and the CVAE. The latter consists of the encoder and the decoder. The label “Res Block” refers to a residual block, and “Res Block x6” indicates the stacking of six Res Blocks. As in the typical implementation of VAEs,⁷ the variance output is regarded as $\ln V$ because neural networks can generally output both positive and negative values. Consequently, $\mathbf{a}_{HR} + \epsilon^T \exp[1/2 \ln V]$ provides a realization of the true state $\hat{\mathbf{z}}$ in Eq. (14c).

this replacement slightly decreases the inference accuracy. This result is due to the experimental setup where the synthetic observations were generated by subsampling (Section V B); that is, the observation operator is linear. Although the proposed SRDA can theoretically address nonlinear observation operators (Section IV), such a nonlinear case is not examined in this proof of concept,

which remains a topic for future research.

In preprocessing, the vorticity ω at each grid point is transformed by

$$\text{clip}_{[0,1]} \left(\frac{\omega - m_\omega}{s_\omega} \right). \quad (21)$$

The clipping function, $\text{clip}_{[0,1]}(z) = \min\{1, \max\{0, z\}\}$ ($z \in \mathbb{R}$), restricts the value range to the interval $[0, 1]$. The parameters m_ω and s_ω are determined such that 99.9% of the vorticity values fall within the $[0, 1]$ range. After applying Eq. (21), zero is assigned to the HR grid points without observations, and zero is regarded as a missing value. This clear interpretation of zero facilitates feature extraction from input data.³⁴

D. Training and testing methods for the neural networks

1. Training method

We adopted an offline strategy in which training data are pre-generated [Fig. 6(a)]. The training data consist of pairs of HR observations and LR forecasts, as discussed in Section IV E. The initial conditions for the LR fluid model were obtained by applying a low-pass filter to the HR simulation results in the wavenumber domain. After time integration over $\Delta T = 1$, the resultant LR forecasts were used in training. This ΔT equals the assimilation interval, as explained below, which is a reasonable timescale because $\Delta T = 1$ is approximately half of the advection time of the zonal jet. The corresponding observations were obtained by subsampling and adding Gaussian noise (Section V B). Figure 6(a) denotes pairs of the LR forecast and the HR observations as stars. By varying the random initial perturbations (Section V A), we conducted 4,500 simulations; 70% were used as training data and the remaining 30% as validation data for hyperparameter tuning.

In principle, no HR simulation is required because the training data include LR forecasts rather than HR results (Sections IV D and IV E). These LR forecasts are obtained by numerical integration in which the analysis states are used as initial conditions. In offline training, however, such an analysis is unavailable because the CVAE is not trained yet. In realistic applications, these initial conditions can be given from existing assimilated data, such as reanalysis,^{67,68} or online training will be effective,⁶⁹ where neural-network training and data generation are executed alternately.

The SR model was trained, followed by training the CVAE. During the CVAE training, all parameters in the SR model were fixed, as discussed in Section IV E. The loss functions of the SR model and the CVAEs are l_{SR} in Eq. (18) and l_{SRDA} in Eq. (13), respectively. The CVAE

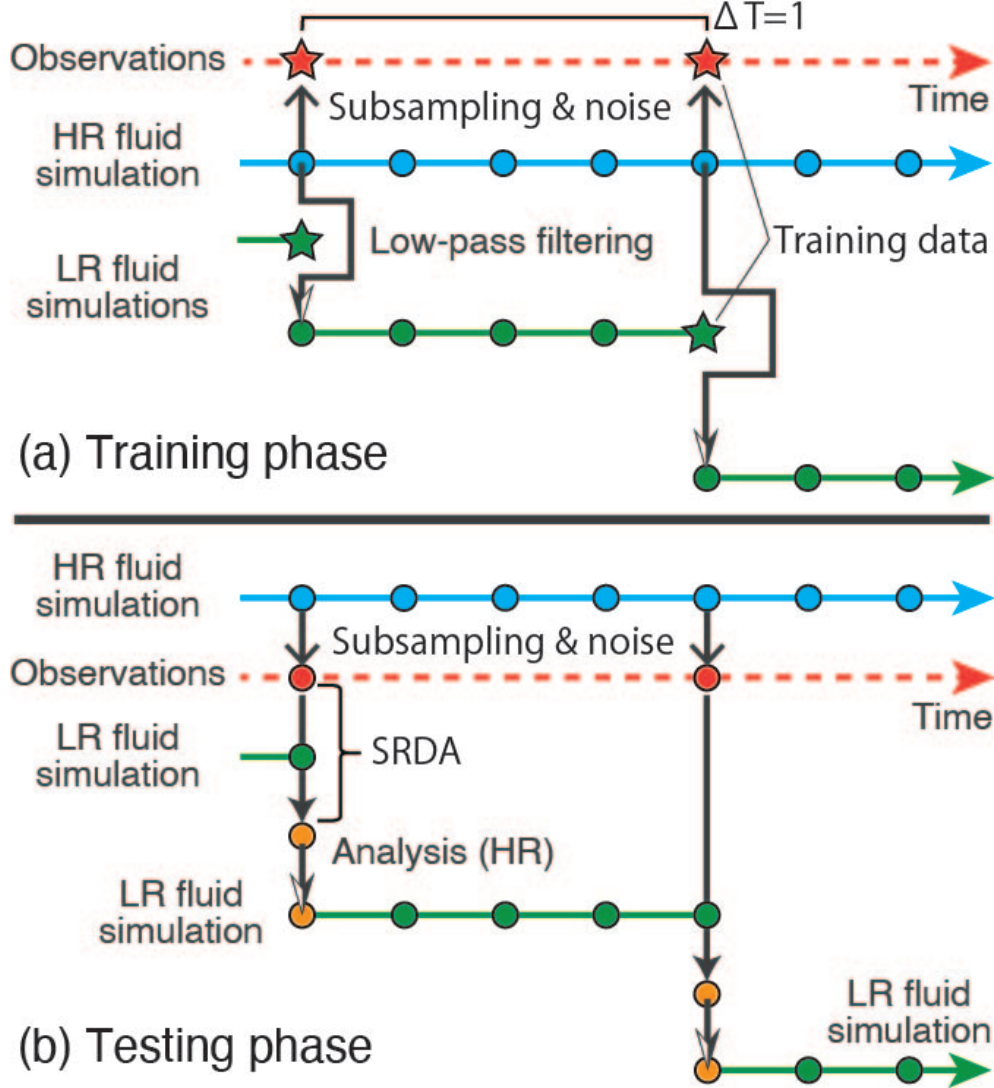


FIG. 6. Schematics of time series for (a) training and (b) testing phases. The assimilation interval is set to $\Delta T = 1$, while the output interval (i.e., the forecast interval) is $\Delta T/4 = 0.25$.

and the SR model were trained using the Adam optimizer⁷⁰ with a learning rate of 1×10^{-4} and a mini-batch size of 128. Each training was terminated using early stopping with a patience parameter of 50 epochs. The parameters in l_{SRDA} were set to $r = 1.2 \times 10^{-5}$ and $b = 1.0 \times 10^{-3}$. The value of r was given by the variance of the measurement errors (Section V B), while b was determined through grid search to balance the reconstruction error and the KL divergence in the ELBO. Without this balancing, the performance of the CVAE would deteriorate. This phenomenon is often observed in VAEs,^{71,72} and the loss balancing can be optimized during training.⁷³ For simplicity, however, such an advanced technique was not employed in the present study.

2. Testing method

The sequential SRDA was tested using the method described in Section IV F. Figure 6(b) shows a schematic of the test phase. The only difference between Figs. 4 and 6(b) is that observations are generated by subsampling the HR simulation results. Due to this difference, the HR results are regarded as the ground truth, and the SRDA can be evaluated by comparing its inference to the ground truth. We newly conducted 500 HR fluid simulations. For each case, the LR fluid model was initialized with the low-pass filtered HR vorticity at $t = 0$; the SRDA was subsequently conducted until $t = 20$ with the assimilation interval $\Delta T = 1$. Without SRDA, the vorticity evolution would differ from the ground truth, not only due to the difference in the initial condition (i.e., all high-wavenumber components are removed), but also due to the difference in the fluid model resolution (i.e., LR versus HR).

Two test metrics were used to assess pixel-wise accuracy and pattern consistency, both of which measure deviations from the ground truth. The mean absolute error (MAE) ratio quantifies pixel-wise errors.

$$\text{MAE ratio} = \frac{\sum_i |\omega_i - \hat{\omega}_i|}{\sum_i |\omega_i|}, \quad (22)$$

where the summation is taken over all grid points, ω_i denotes the ground-truth vorticity at the i -th grid point, and $\hat{\omega}_i$ is the corresponding inference. The mean structural similarity index measure (MSSIM) loss evaluates the consistency of spatial patterns:⁷⁴

$$\begin{aligned} \text{MSSIM loss} &= 1 - \text{MSSIM}, \\ &= 1 - \sum_i \frac{(2\mu_i\hat{\mu}_i + C_1^2)(2\gamma_i + C_2^2)}{(\mu_i^2 + \hat{\mu}_i^2 + C_1^2)(\sigma_i^2 + \hat{\sigma}_i^2 + C_2^2)}, \end{aligned} \quad (23)$$

where $C_1 = 0.01$, $C_2 = 0.03$, μ_i and σ_i^2 are the mean and variance of the ground truth, respectively, $\hat{\mu}_i$ and $\hat{\sigma}_i^2$ are the corresponding quantities for the inference, and γ_i is the covariance between the ground truth and the inference. The variables in the summation are calculated locally in space using a Gaussian filter. The MSSIM loss takes a value greater than or equal to 0; a smaller value indicates spatial patterns more similar to the ground truth. A detailed discussion of MSSIM can be found in Wang et al.⁷⁴

The MAE ratio and MSSIM loss were calculated at each time step in each test simulation. The values averaged across all test simulations are referred to by the same names. Both MAE ratio and MSSIM loss are collectively called the test errors.

E. Baseline model using Ensemble Kalman Filter (EnKF)

As a comparison to the SRDA, we employed an ensemble Kalman filter (EnKF)⁷⁵ for the LR fluid model, using the perturbed observation method.⁷⁶ The choice of EnKF was motivated by its ability to estimate uncertainty through ensemble simulations. The uncertainty with the EnKF is compared with that with the SRDA.

Assimilation was conducted in the HR space after the LR forecast was super-resolved to the HR using bicubic interpolation, where the assimilation interval $\Delta T = 1$ is the same as in the SRDA. Barthélémy et al.³⁹ argued that performing the EnKF in the HR space can yield more accurate inferences than those in the LR space when observations are defined at HR grid points. Furthermore, this approach clarifies the comparison with the SRDA because both EnKF and SRDA employ the LR fluid model and perform DA in the HR space.

The background error covariance matrices were spatially localized using a function proposed by Gaspari and Cohn.⁷⁷ These error covariances were inflated by adding Gaussian noise to the analysis, prior to the forecast process.⁷⁸ This Gaussian noise incorporates spatial correlation by estimating its covariance from the training data at each time step. The initial perturbations for creating ensemble members were also drawn from this Gaussian distribution. We confirmed that the results are not sensitive to the statistics of the Gaussian noise for inflation. Indeed, similar results were obtained when the Gaussian noise had a constant correlation length.

Hyperparameters for the EnKF were adjusted using the training data to minimize the MAE. Specifically, the following parameters were tuned: the number of ensemble members (set to 300 after tuning), the amplitude of the initial perturbation for generating ensemble members, the amplitude of the additive inflation, the localization radius, and the amplitude for perturbing observations. The full implementation of the EnKF is also available at our GitHub repository (see Data Availability Statement).

VI. RESULTS AND DISCUSSION

A. Time evolution of vorticity in the jet system

Before discussing the SRDA results, we describe the time evolution of HR vorticity in the jet system and confirm the sensitivity to initial conditions (i.e., a positive Lyapunov exponent).

Figure 7 shows a typical evolution of HR vorticity. Initially ($t = 0$), an unstable jet exists around

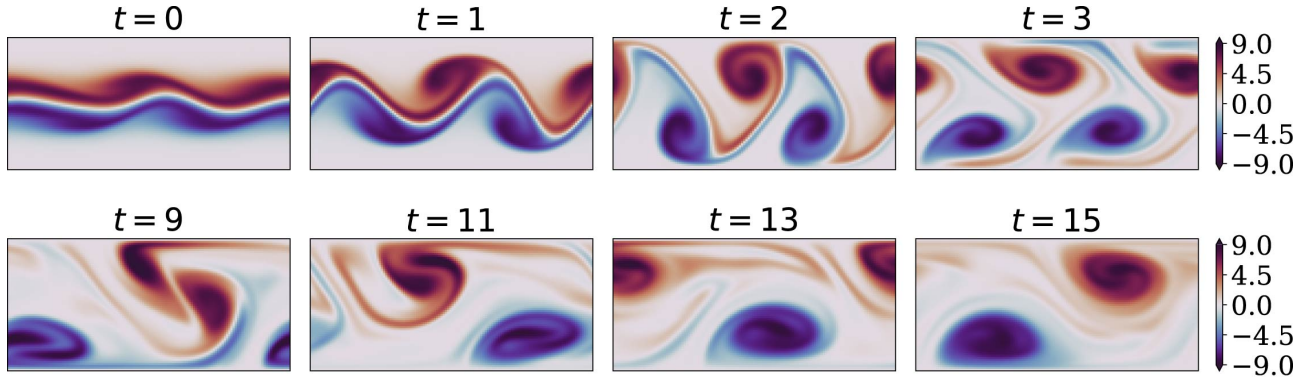


FIG. 7. Typical vorticity evolution from the HR ground-truth data.

the y center with small perturbations. The jet starts meandering and breaks down into multiple vortices, accompanied by the development of fine filaments ($1 \lesssim t \lesssim 4$). Subsequently, vortex merging occurs, intensifying small-scale structures again ($4 \lesssim t \lesssim 12$). Finally, a wavenumber-1 structure continues to propagate westward ($12 \lesssim t$). This final state is statistically steady and can be understood by Rossby wave dynamics.⁵⁶

We confirmed that the maximum Lyapunov exponent λ is positive: $\lambda = 3.11$. This suggests that the temporal evolution of vorticity exhibits initial-value sensitivity, likely due to the barotropic instability of the initial conditions. Indeed, without DA, the deviation from the ground truth continues to increase over time, while the SRDA effectively suppresses this error growth (Section VIC).

B. Accuracy of SR

We first confirm the accuracy of inference by the SR model, as the SRDA is based on this model. Figure 8 shows three sets of snapshots for the ground truth, observations, LR input, and SR output. The results indicate that the SR model reproduces the fine filaments and small-scale structures within vortices. These patterns are not evident in the LR inputs or observations.

Flow-field reconstruction has been extensively studied using neural networks.^{79–82} In these studies, inputs are incomplete, such as spatially sparse sensor measurements, where only a portion of the entire domain is available. Neural networks are then trained by comparing their output to complete target data. The setup of our problem is opposite to that of these studies: in our case, the input is complete, while the target (i.e., the observation) is incomplete.

The success of the SR in our study is attributable to two factors: (i) the point-wise nature of

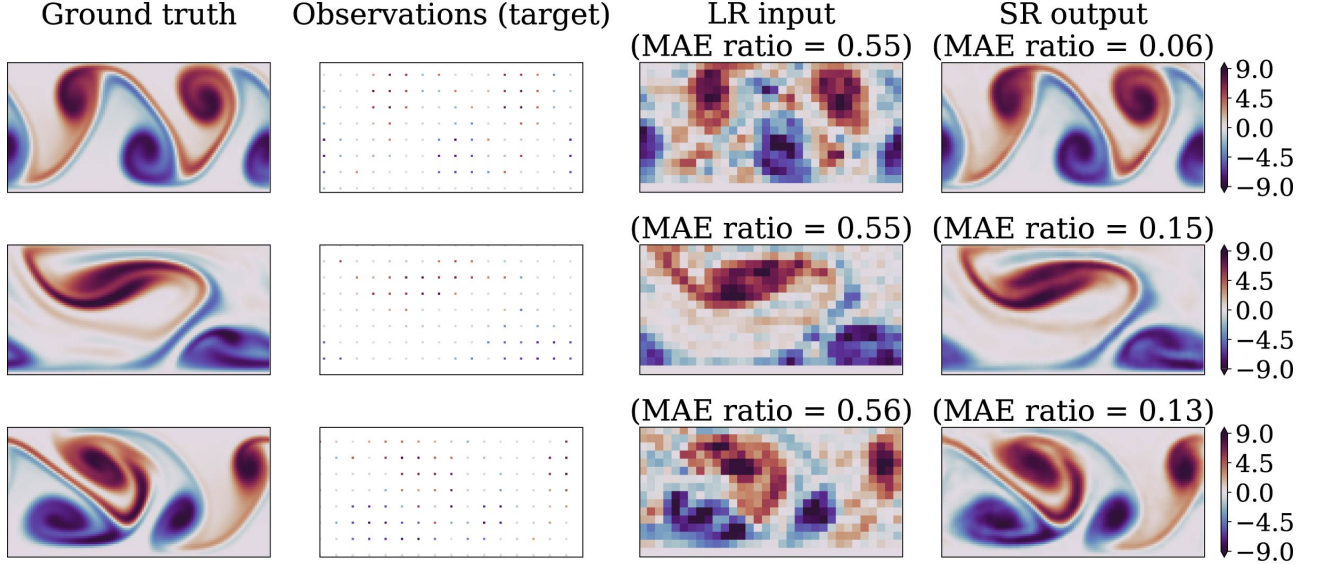


FIG. 8. Vorticity snapshots for the ground truth, observations, LR input, and SR output. The SR model was trained using the observation data as target. The input data are not indexed by time because each sample was randomly selected for testing without simulating time evolution.

the loss function and (ii) the weight sharing of convolution. The loss function l_{SR} in Eq. (18) operates at individual grid points, and only the non-missing observed points contribute to l_{SR} . This property enables backpropagation even when the target data are missing, as discussed in Section IV D. Furthermore, since convolution shares its kernel across the space (known as weight sharing),⁸³ the efficient learning was realized using the small amount of non-missing observational data.

Although the inference appears to be accurate, we confirmed that the SR model cannot adequately correct forecast errors. One might think that the SR output could be used as the analysis due to its high accuracy (Fig. 8). However, we found that test errors accumulated over time when the downsampled SR output was used as the initial condition for the LR fluid model. This result indicates that observations need to be assimilated into forecasts.

C. Accuracy of LR forecast by SRDA

We demonstrate that the sequential SRDA can make more accurate inferences than the EnKF. The LR forecast is compared in this section, and the HR analysis is examined next (Section VI D).

Figure 9 shows snapshots of the ground truth and forecasts for the EnKF and the SRDA. To

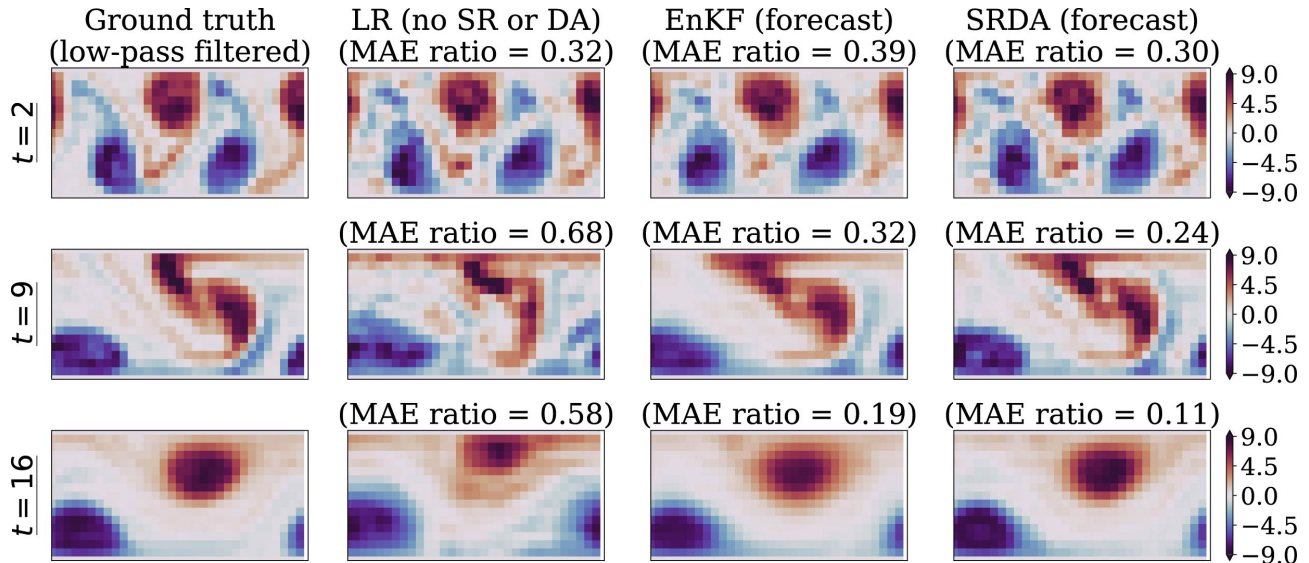


FIG. 9. Vorticity snapshots of the ground truth and forecasts for the EnKF and the SRDA at $t = 2, 9,$ and 16 . For comparison, the figure also shows LR simulation results without SR or DA. A low-pass filter was applied to the ground-truth snapshots to align the resolution to the LR.

align the resolution, a low-pass filter was applied to the HR ground-truth vorticity. The figure also includes LR simulation results without SR or DA. During the jet collapse ($t = 2$), differences in the inferences are not obvious, likely because the LR fluid model cannot well emulate fine filaments. During the vortex merging ($t = 9$), the SRDA most accurately describes the vortex-split distribution near the center. The EnKF also captures this pattern, but the SRDA inference is closer to the ground truth. Without SR or DA, the vortex-split structure is not reproduced. In the steady state ($t = 16$), both EnKF and SRDA accurately infer the vorticity phase. Without SR or DA, the vortex shapes and locations still differ from the ground truth.

The quantitative analysis further confirms the accuracy of the SRDA forecast. The top panels in Fig. 10 show the time series of the mean values for the MAE ratio and the MSSIM loss. Without SR or DA (green dotted lines), the test errors increase over time due to the sensitivity to initial conditions (i.e., the positive Lyapunov exponent in Section VIA). In contrast, this error growth is suppressed by the EnKF (orange dashed lines) and the SRDA (blue solid lines). The error reduction occurs every time unit since the assimilation interval was set to 1. When averaged over time, both time series have two peaks, corresponding to the two developments of small-scale patterns by the jet collapse ($t \sim 2$) and the vortex merging ($t \sim 9$). The bottom panels in Fig. 10 show the differences in the test errors between the SRDA and the EnKF, where the gray areas

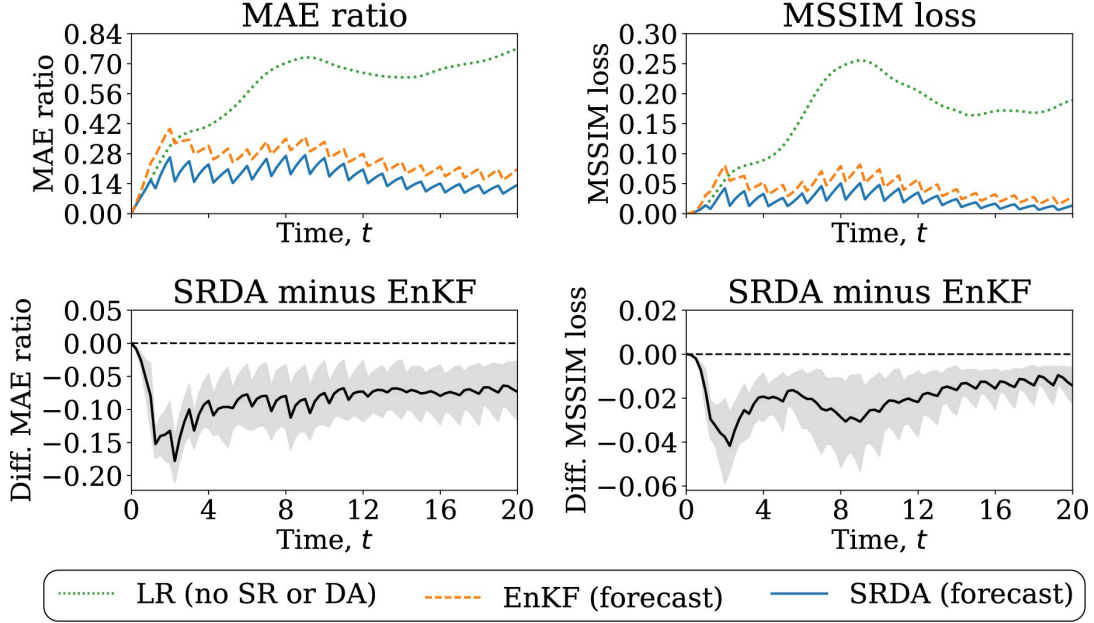


FIG. 10. Time series of the MAE ratio and the MSSIM loss for the forecast states in the 500 test simulations. The top panels show the mean test errors at each time step with an output interval of 0.25. The bottom panels show the differences between the SRDA and the EnKF, where the gray areas cover the 10th to 90th percentile values and the solid lines indicate the mean differences.

represent the 10th to 90th percentile values. The test errors of the SRDA are significantly smaller than those of the EnKF. Thus, we can conclude that the SRDA forecast outperforms the EnKF in terms of pixel-wise accuracy and pattern consistency.

Within the SRDA framework, the LR forecast can be super-resolved to the HR at an arbitrary time by the SR model (Section IV F). Figure 11 shows a typical vortex merging between $t = 8.5$ and 11.0 from the ground truth, the LR forecast, and the super-resolved forecast. The merging of two vortices is not obvious in the LR, but is well captured in the super-resolved forecast.

D. Accuracy of HR analysis by SRDA

We next demonstrate the accuracy of the HR analysis provided by the SRDA. Figure 12 shows snapshots of the ground truth and analyses. During the jet collapse ($t = 2$), the filament structure appears much more distinct in the SRDA analysis than in the EnKF. Furthermore, during the vortex merging ($t = 9$ and 11), the SRDA snapshots exhibit sharper vortex shapes and clearer internal structures compared to the EnKF.

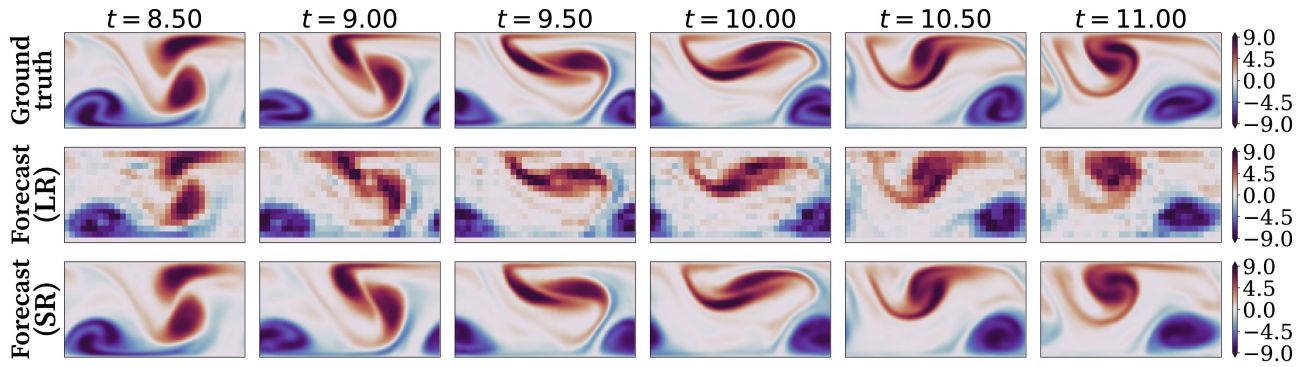


FIG. 11. Typical vortex merging in the ground truth, the LR forecasts, and the super-resolved forecast.

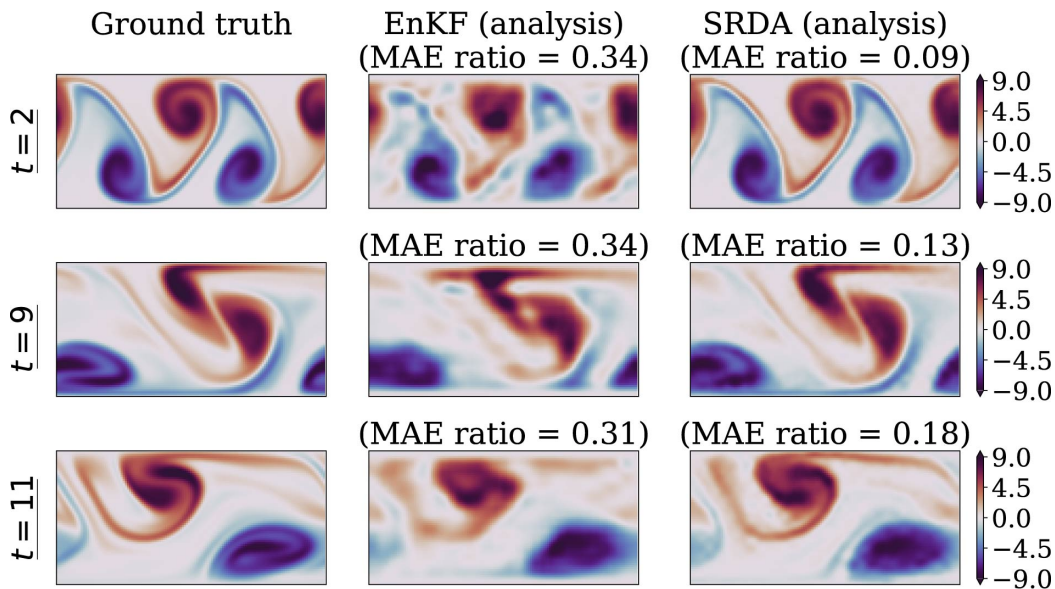


FIG. 12. Vorticity snapshots of the ground truth and analyses for the EnKF and the SRDA at $t = 2, 9,$ and 11 .

The quantitative analysis also confirms the accuracy of the SRDA analysis. Figure 13 shows the time series of the MAE ratio and the MSSIM loss, as in Fig. 10. The dots represent the assimilation time steps, with assimilation intervals at 1. The SRDA and EnKF analyses are inferred only at these times. The EnKF time series (orange dashed lines) show two peaks, corresponding to the two developments of small-scale patterns linked to the jet collapse ($t \sim 2$) and the vortex merging ($t \sim 9$). These peaks are less apparent in the SRDA time series (blue solid lines), especially for the first peak. This result suggests that the SRDA effectively mitigates the error increase during the jet collapse. The bottom panels in Fig. 13 indicate that the MAE ratio and the MSSIM loss for the SRDA are significantly smaller than those of the EnKF. Thus, we can conclude that the SRDA

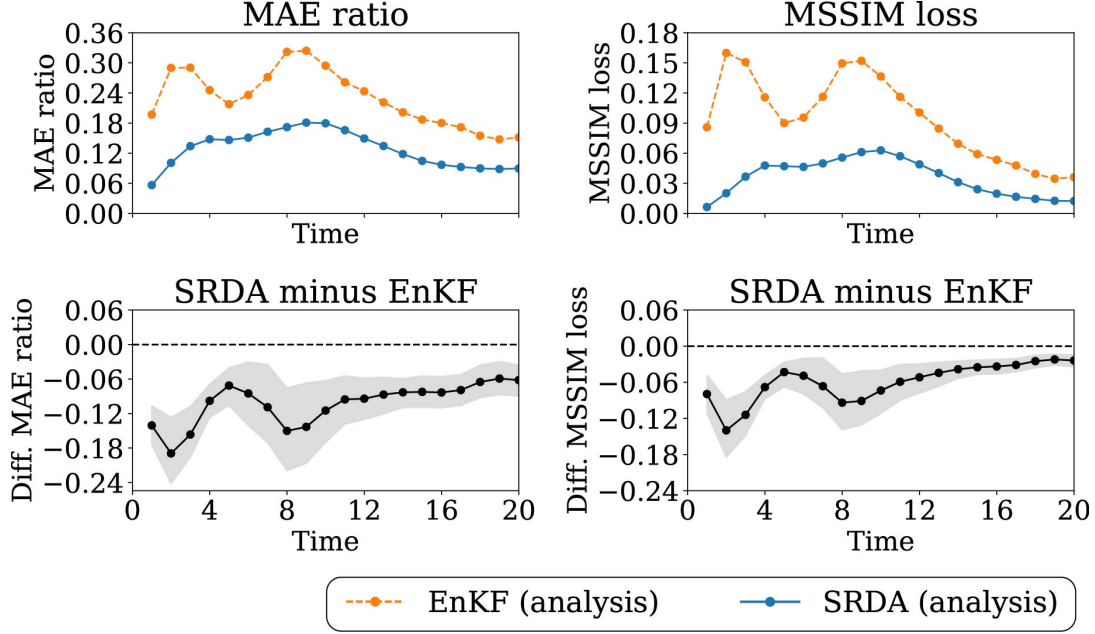


FIG. 13. Time series of the MAE ratio and the MSSIM loss for the analysis states in the 500 test simulations. These states were inferred only at the analysis time steps, denoted by dots. The top panels show the mean test errors. The bottom panels show the differences between the SRDA and the EnKF, where the gray areas cover the 10th to 90th percentile values and the solid lines indicate the mean differences.

analysis is more accurate than the EnKF analysis, in line with the forecast results (Section VI C).

We compare uncertainties estimated by the EnKF and the SRDA. Here, standard deviation (SD) is used as an indicator of uncertainty. For the SRDA, SD was directly calculated by taking the square root of the estimated variances in Eq. (12), while for the EnKF, SD at each grid point was calculated from all ensemble members (i.e., 300 members).

Figure 14 compares distributions of the analysis values and their SDs for the EnKF and the SRDA. The SRDA SD tends to be large around vortex filaments or vortex edges. This tendency appears to be most evident in the jet collapse ($t = 2$). The EnKF SD also exhibits a similar tendency; however, the SD distribution is blurred, likely reflecting the blurred vortex patterns. The SD value ranges also differ: the EnKF SD is between 0.3 and 0.9, while the SRDA SD is between 0.8 and 0.9. Related to this range difference, the SRDA tends to overestimate SD in regions where vorticity is close to zero, which can be found at $t = 9$ and 11 in Fig. 14. In contrast, the EnKF SD tends to be small in small-vorticity regions. This overestimation of the SRDA may be due to a simplified variance estimation in the present CVAE (Section V C), where the variances are computed using the SR model from the LR analysis. Therefore, although the SRDA demonstrated

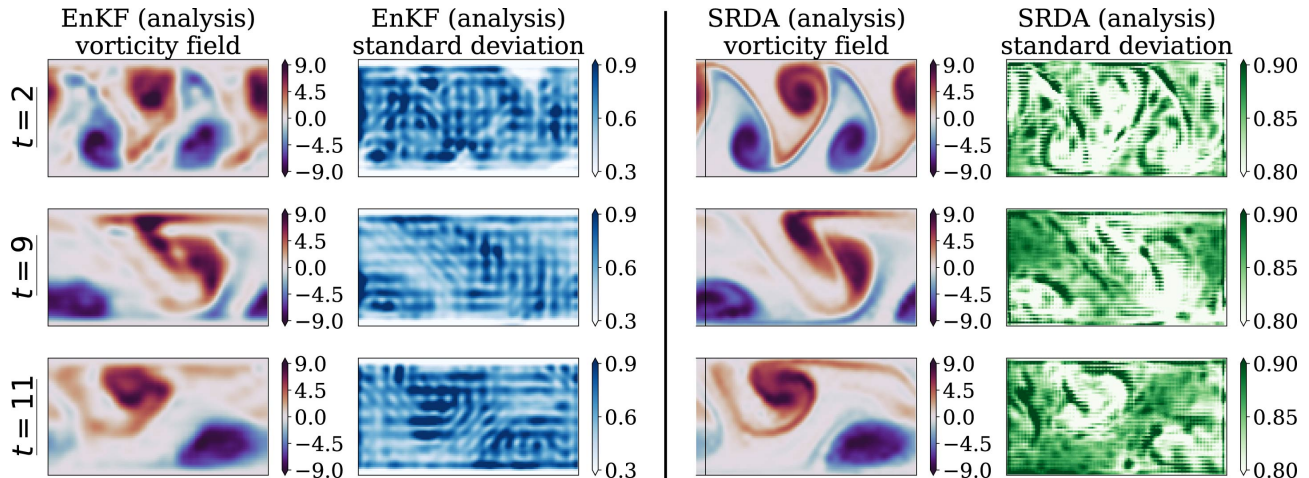


FIG. 14. Vorticity snapshots of the analyses and their standard deviations (SDs) for the EnKF and the SRDA at $t = 2, 9$ and 11 . The analyses shown here are the same as in Fig. 12. To compare them with their SDs, these panels are displayed again.

the potential for uncertainty quantification without relying on ensemble calculation, further model development is necessary. Recent studies demonstrate that VAEs can learn error distributions of model forecasts,^{20–23} and their model architectures may be effective for the SRDA.

E. Computation time of SRDA

Lastly, we confirm that the computational time of the SRDA is much less than that of the EnKF. The elapsed times for the simulations from $t = 0$ to 20 were measured using a single process on a CPU (Intel Xeon Gold 6326). For the SRDA, in addition to the assimilation by the encoder, the LR forecast was super-resolved by the SR model at every output time step ($\Delta t = 0.25$). The average wall time was 21.3 s for the SRDA, considerably less than 205.7 s for the EnKF. This difference is mainly due to the calculation of the ensemble evolution, which is not required in the SRDA.

VII. CONCLUSIONS

This study has proposed a theory of unsupervised SRDA using the CVAE. We have shown that a new DA framework using the ELBO encompasses the 3D-Var formalism (Section III). Since ELBO serves as the loss function for CVAEs, the assimilation can be executed using the CVAE. In this process, it is essential to use a non-diagonal background error covariance matrix to incorporate

the spatial correlations of forecast states into the CVAE, similar to the 3D-Var. Instead of using such non-diagonal matrices, we have further extended the framework by using the non-local nature of SR operations to achieve DA (Section IV). In other words, SR operators can serve as background error covariance matrices. This result provides a theoretical foundation for combining SR and DA.

The combination of SR models and CVAEs enables the assimilation of HR observations into LR forecasts that are computed with LR fluid models. This approach eliminates the need for numerical integration using HR fluid models, thereby reducing computational burden. Specifically, the CVAE’s encoder estimates the HR analysis from the input of LR forecasts and HR observations, while the decoder acts as the observation operator and reconstructs the HR observations from the estimated HR analysis. The resulting HR analysis is then downsampled to the LR using algebraic methods, such as linear interpolation, serving as the initial condition for the LR fluid model in the next assimilation cycle.

The effectiveness of the proposed method was evaluated through numerical experiments using an idealized barotropic ocean jet system (Sections V and VI). Compared to the EnKF, the SRDA demonstrated its ability to obtain accurate HR inferences within shorter computational times. These results suggest the potential of SRDA as an efficient approach for integrating observations into CFD simulations.

There are several future research topics, as SRDA has been recently developed. Although the proposed theory enables learning of nonlinear observation operators, the proof of concept in the present study has examined only the linear observation operator. Furthermore, advanced training methods, such as online training⁶⁹ and loss balancing for VAEs,⁷³ will be important to develop SRDA, whereas a simple offline training method was employed in our study (Section V D). These points will be addressed in a more realistic experimental setup. In practical applications, data partitioning will be important because the data size for three-dimensional flows is larger, which would require the division of snapshots into small patches.^{21,84} Non-Gaussianity is also important in more realistic DA, which has recently been addressed by VAEs²³ and normalizing flows.⁸⁵ The theory proposed in our study will provide a foundation for using such advanced techniques, leading to further development of SRDA.

ACKNOWLEDGMENTS

This work used computational resources of the TSUBAME3.0 supercomputer provided by the Institute of Science Tokyo through the HPCI System Research Project (Project ID: hp220102) to conduct the CFD simulations. The deep learning was performed on the Earth Simulator system (Project IDs: 1-23007 and 1-24009) at the Japan Agency for Marine-Earth Science and Technology (JAMSTEC). This paper is based on results obtained from a project, JPNP22002, commissioned by the New Energy and Industrial Technology Development Organization (NEDO).

DATA AVAILABILITY STATEMENT

The data and source code that support the findings of this study are preserved and openly available at <https://github.com/YukiYasuda2718/srda-cvae>.

Appendix: Hyperparameters of the SR model and the CVAE

We list here the hyperparameters of the SR model and the CVAE shown in Fig. 5. Table II lists the hyperparameters for the convolution layers in the SR model and the CVAE. The kernel size of all convolutions is 3. The slope of all leaky ReLU⁶⁶ is -0.01 . The upscale factor of all pixel shuffle operations⁶⁴ is 2. The resizing in the SR model is performed by bicubic interpolation. The weight parameters of all convolution layers are randomly initialized using uniform distributions.⁸⁶

REFERENCES

- ¹M. Asch, M. Bocquet, and M. Nodet, *Data Assimilation* (Society for Industrial and Applied Mathematics, Philadelphia, PA, 2016) <https://epubs.siam.org/doi/pdf/10.1137/1.9781611974546>.
- ²A. Carrassi, M. Bocquet, L. Bertino, and G. Evensen, “Data assimilation in the geosciences: An overview of methods, issues, and perspectives,” *WIREs Climate Change* **9**, e535 (2018), <https://wires.onlinelibrary.wiley.com/doi/pdf/10.1002/wcc.535>.
- ³H. D. I. Abarbanel, P. J. Rozdeba, and S. Shirman, “Machine Learning: Deepest Learning as Statistical Data Assimilation Problems,” *Neural Computation* **30**, 2025–2055 (2018), https://direct.mit.edu/neco/article-pdf/30/8/2025/1047132/neco_a_01094.pdf.

TABLE II. Hyperparameters for the convolution layers in the SR model and the CVAE. The layer names are defined in Fig. 5.

Layer name	Input channels	Output channels	Stride
Conv2D-0	1	128	1
Conv2D-1	128	128	1
Conv2D-2	128	512	1
Conv2D-3	128	256	1
Conv2D-4	256	1024	1
Conv2D-5	256	256	1
Conv2D-6	256	1	1
Conv2D-7	1	32	1
Conv2D-8	256	1	1
Conv2D-9	256	1	1
Conv2D-10	1	8	1
Conv2D-11	8	8	1
Conv2D-12	8	1	1
Conv2D-13	1	112	2
Conv2D-14	112	112	1
Conv2D-15	112	224	2
Conv2D-16	224	224	1
Conv2D-17	256	256	1

⁴R. T. Q. Chen, Y. Rubanova, J. Bettencourt, and D. Duvenaud, “Neural ordinary differential equations,” in *Proceedings of the 32nd International Conference on Neural Information Processing Systems*, NIPS’18 (Curran Associates Inc., Red Hook, NY, USA, 2018) p. 6572–6583.

⁵A. J. Geer, “Learning earth system models from observations: machine learning or data assimilation?” *Philosophical Transactions of the Royal Society A: Mathematical, Physical and Engineering Sciences* **379**, 20200089 (2021), <https://royalsocietypublishing.org/doi/pdf/10.1098/rsta.2020.0089>.

- ⁶M. Bocquet, J. Brajard, A. Carrassi, and L. Bertino, “Bayesian inference of chaotic dynamics by merging data assimilation, machine learning and expectation-maximization,” *Foundations of Data Science* **2**, 55–80 (2020).
- ⁷D. P. Kingma and M. Welling, “An introduction to variational autoencoders,” *Foundations and Trends® in Machine Learning* **12**, 307–392 (2019).
- ⁸F.-A. Croitoru, V. Hondru, R. T. Ionescu, and M. Shah, “Diffusion models in vision: A survey,” *IEEE Transactions on Pattern Analysis and Machine Intelligence* , 1–20 (2023).
- ⁹D. P. Kingma and M. Welling, “Auto-Encoding Variational Bayes,” in *2nd International Conference on Learning Representations, ICLR 2014, Banff, AB, Canada, April 14-16, 2014, Conference Track Proceedings* (2014) <http://arxiv.org/abs/1312.6114v10>.
- ¹⁰D. J. Rezende, S. Mohamed, and D. Wierstra, “Stochastic backpropagation and approximate inference in deep generative models,” in *Proceedings of the 31st International Conference on Machine Learning*, Proceedings of Machine Learning Research, Vol. 32, edited by E. P. Xing and T. Jebara (PMLR, Beijing, China, 2014) pp. 1278–1286.
- ¹¹G. Dong, G. Liao, H. Liu, and G. Kuang, “A review of the autoencoder and its variants: A comparative perspective from target recognition in synthetic-aperture radar images,” *IEEE Geoscience and Remote Sensing Magazine* **6**, 44–68 (2018).
- ¹²D. P. Kingma, D. J. Rezende, S. Mohamed, and M. Welling, “Semi-supervised learning with deep generative models,” in *Proceedings of the 27th International Conference on Neural Information Processing Systems - Volume 2*, NIPS’14 (MIT Press, Cambridge, MA, USA, 2014) p. 3581–3589.
- ¹³K. Sohn, H. Lee, and X. Yan, “Learning structured output representation using deep conditional generative models,” in *Advances in Neural Information Processing Systems*, Vol. 28, edited by C. Cortes, N. Lawrence, D. Lee, M. Sugiyama, and R. Garnett (Curran Associates, Inc., 2015).
- ¹⁴M. Liu, D. Grana, and L. P. de Figueiredo, “Uncertainty quantification in stochastic inversion with dimensionality reduction using variational autoencoder,” *Geophysics* **87**, M43–M58 (2021), <https://pubs.geoscienceworld.org/geophysics/article-pdf/87/2/M43/5575417/geo-2021-0138.1.pdf>.
- ¹⁵S. Mohd Razak, A. Jahandideh, U. Djuraev, and B. Jafarpour, “Deep Learning for Latent Space Data Assimilation in Subsurface Flow Systems,” *SPE Journal* **27**, 2820–2840 (2022), <https://onepetro.org/SJ/article-pdf/27/05/2820/3015238/spe-203997-pa.pdf>.

- ¹⁶Melinc, Boštjan and Zaplotnik, Žiga, “3d-var data assimilation using a variational autoencoder,” *Quarterly Journal of the Royal Meteorological Society* **150**, 2273–2295 (2024), <https://rmets.onlinelibrary.wiley.com/doi/pdf/10.1002/qj.4708>.
- ¹⁷J. Mack, R. Arcucci, M. Molina-Solana, and Y.-K. Guo, “Attention-based convolutional autoencoders for 3d-variational data assimilation,” *Computer Methods in Applied Mechanics and Engineering* **372**, 113291 (2020).
- ¹⁸S. Cheng, I. C. Prentice, Y. Huang, Y. Jin, Y.-K. Guo, and R. Arcucci, “Data-driven surrogate model with latent data assimilation: Application to wildfire forecasting,” *Journal of Computational Physics* **464**, 111302 (2022).
- ¹⁹S. Cheng, Y. Zhuang, L. Kahouadji, C. Liu, J. Chen, O. K. Matar, and R. Arcucci, “Multi-domain encoder–decoder neural networks for latent data assimilation in dynamical systems,” *Computer Methods in Applied Mechanics and Engineering* **430**, 117201 (2024).
- ²⁰I. Grooms, “Analog ensemble data assimilation and a method for constructing analogs with variational autoencoders,” *Quarterly Journal of the Royal Meteorological Society* **147**, 139–149 (2021), <https://rmets.onlinelibrary.wiley.com/doi/pdf/10.1002/qj.3910>.
- ²¹L. M. Yang and I. Grooms, “Machine learning techniques to construct patched analog ensembles for data assimilation,” *Journal of Computational Physics* **443**, 110532 (2021).
- ²²I. Grooms, C. Renaud, Z. Stanley, and L. M. Yang, “Analog ensemble data assimilation in a quasigeostrophic coupled model,” *Quarterly Journal of the Royal Meteorological Society* **149**, 1018–1037 (2023), <https://rmets.onlinelibrary.wiley.com/doi/pdf/10.1002/qj.4446>.
- ²³Y. Xiao, Q. Jia, W. Xue, and L. Bai, “Vae-var: Variational-autoencoder-enhanced variational assimilation,” (2024), arXiv:2405.13711 [cs.LG].
- ²⁴A. C. Lorenc, “Analysis methods for numerical weather prediction,” *Quarterly Journal of the Royal Meteorological Society* **112**, 1177–1194 (1986), <https://rmets.onlinelibrary.wiley.com/doi/pdf/10.1002/qj.49711247414>.
- ²⁵V. K. Ha, J.-C. Ren, X.-Y. Xu, S. Zhao, G. Xie, V. Masero, and A. Hussain, “Deep learning based single image super-resolution: A survey,” *International Journal of Automation and Computing* (2019), 10.1007/s11633-019-1183-x.
- ²⁶S. Anwar, S. Khan, and N. Barnes, “A deep journey into super-resolution: A survey,” *ACM Comput. Surv.* **53** (2020), 10.1145/3390462.
- ²⁷A. Ducournau and R. Fablet, “Deep learning for ocean remote sensing: an application of convolutional neural networks for super-resolution on satellite-derived sst data,” (2016) pp. 1–6.

- ²⁸T. Vandal, E. Kodra, S. Ganguly, A. Michaelis, R. Nemani, and A. R. Ganguly, “DeepSD: Generating high resolution climate change projections through single image super-resolution,” (Association for Computing Machinery, 2017) pp. 1663–1672.
- ²⁹R. Onishi, D. Sugiyama, and K. Matsuda, “Super-resolution simulation for real-time prediction of urban micrometeorology,” *SOLA* **15**, 178–182 (2019).
- ³⁰K. Fukami, K. Fukagata, and K. Taira, “Super-resolution reconstruction of turbulent flows with machine learning,” *Journal of Fluid Mechanics* **870**, 106–120 (2019).
- ³¹C. Wang, E. Bentinegna, W. Zhou, L. Klein, and B. Elmegreen, “Physics-informed neural network super resolution for advection-diffusion models,” in *Third Workshop on Machine Learning and the Physical Sciences (NeurIPS 2020)* (2020).
- ³²J. Wang, Z. Liu, I. Foster, W. Chang, R. Kettimuthu, and V. R. Kotamarthi, “Fast and accurate learned multiresolution dynamical downscaling for precipitation,” *Geoscientific Model Development* **14**, 6355–6372 (2021).
- ³³Y. Yasuda, R. Onishi, Y. Hirokawa, D. Kolomenskiy, and D. Sugiyama, “Super-resolution of near-surface temperature utilizing physical quantities for real-time prediction of urban micrometeorology,” *Building and Environment* **209**, 108597 (2022).
- ³⁴Y. Yasuda, R. Onishi, and K. Matsuda, “Super-resolution of three-dimensional temperature and velocity for building-resolving urban micrometeorology using physics-guided convolutional neural networks with image inpainting techniques,” *Building and Environment* , 110613 (2023).
- ³⁵J. McGibbon, S. K. Clark, B. Henn, A. Kwa, O. Watt-Meyer, W. A. Perkins, and C. S. Bretherton, “Global precipitation correction across a range of climates using cycleGAN,” *Geophysical Research Letters* **51**, e2023GL105131 (2024), e2023GL105131 2023GL105131, <https://agupubs.onlinelibrary.wiley.com/doi/pdf/10.1029/2023GL105131>.
- ³⁶K. Fukami, K. Fukagata, and K. Taira, “Super-resolution analysis via machine learning: A survey for fluid flows,” *Theoretical and Computational Fluid Dynamics* **37**, 421–444 (2023).
- ³⁷C. Dong, C. C. Loy, K. He, and X. Tang, “Learning a deep convolutional network for image super-resolution,” in *Computer Vision – ECCV 2014*, edited by D. Fleet, T. Pajdla, B. Schiele, and T. Tuytelaars (Springer International Publishing, Cham, 2014) pp. 184–199.
- ³⁸J. Gu and C. Dong, “Interpreting super-resolution networks with local attribution maps,” in *Proceedings of the IEEE/CVF Conference on Computer Vision and Pattern Recognition (CVPR)* (2021) pp. 9199–9208.

- ³⁹S. Barthélémy, J. Brajard, L. Bertino, and F. Counillon, “Super-resolution data assimilation,” *Ocean Dynamics* **72**, 661–678 (2022).
- ⁴⁰Y. Yasuda and R. Onishi, “Spatio-temporal super-resolution data assimilation (srda) utilizing deep neural networks with domain generalization,” *Journal of Advances in Modeling Earth Systems* **15**, e2023MS003658 (2023), e2023MS003658 2023MS003658, <https://agupubs.onlinelibrary.wiley.com/doi/pdf/10.1029/2023MS003658>.
- ⁴¹K. Imaoka, M. Kachi, H. Fujii, H. Murakami, M. Hori, A. Ono, T. Igarashi, K. Nakagawa, T. Oki, Y. Honda, and H. Shimoda, “Global change observation mission (gcom) for monitoring carbon, water cycles, and climate change,” *Proceedings of the IEEE* **98**, 717–734 (2010).
- ⁴²M. Durand, L.-L. Fu, D. P. Lettenmaier, D. E. Alsdorf, E. Rodriguez, and D. Esteban-Fernandez, “The surface water and ocean topography mission: Observing terrestrial surface water and oceanic submesoscale eddies,” *Proceedings of the IEEE* **98**, 766–779 (2010).
- ⁴³R. Cifelli, V. Chandrasekar, H. Chen, and L. E. Johnson, “High resolution radar quantitative precipitation estimation in the san francisco bay area: Rainfall monitoring for the urban environment,” *Journal of the Meteorological Society of Japan. Ser. II* **96A**, 141–155 (2018).
- ⁴⁴Z. Li, J. Wang, and L.-L. Fu, “An observing system simulation experiment for ocean state estimation to assess the performance of the swot mission: Part 1—a twin experiment,” *Journal of Geophysical Research: Oceans* **124**, 4838–4855 (2019), <https://agupubs.onlinelibrary.wiley.com/doi/pdf/10.1029/2018JC014869>.
- ⁴⁵T. Honda, A. Amemiya, S. Otsuka, G.-Y. Lien, J. Taylor, Y. Maejima, S. Nishizawa, T. Yamaura, K. Sueki, H. Tomita, S. Satoh, Y. Ishikawa, and T. Miyoshi, “Development of the real-time 30-s-update big data assimilation system for convective rainfall prediction with a phased array weather radar: Description and preliminary evaluation,” *Journal of Advances in Modeling Earth Systems* **14**, e2021MS002823 (2022), e2021MS002823 2021MS002823, <https://agupubs.onlinelibrary.wiley.com/doi/pdf/10.1029/2021MS002823>.
- ⁴⁶J. T. Ormerod and M. P. Wand, “Explaining variational approximations,” *The American Statistician* **64**, 140–153 (2010), <https://doi.org/10.1198/tast.2010.09058>.
- ⁴⁷J. Zhu, N. Chen, and E. P. Xing, “Bayesian inference with posterior regularization and applications to infinite latent svms,” *Journal of Machine Learning Research* **15**, 1799–1847 (2014).
- ⁴⁸S. Ghimire, J. L. Sapp, M. Horacek, and L. Wang, “A variational approach to sparse model error estimation in cardiac electrophysiological imaging,” in *Medical Image Computing and Computer-Assisted Intervention - MICCAI 2017*, edited by M. Descoteaux, L. Maier-Hein,

- A. Franz, P. Jannin, D. L. Collins, and S. Duchesne (Springer International Publishing, Cham, 2017) pp. 745–753.
- ⁴⁹C. M. Bishop, *Pattern Recognition and Machine Learning (Information Science and Statistics)* (Springer-Verlag, Berlin, Heidelberg, 2006).
- ⁵⁰D. Rezende and S. Mohamed, “Variational inference with normalizing flows,” in *Proceedings of the 32nd International Conference on Machine Learning*, Proceedings of Machine Learning Research, Vol. 37, edited by F. Bach and D. Blei (PMLR, Lille, France, 2015) pp. 1530–1538.
- ⁵¹I. Kobyzev, S. D. Prince, and M. A. Brubaker, “Normalizing flows: An introduction and review of current methods,” *IEEE Transactions on Pattern Analysis & Machine Intelligence* **43**, 3964–3979 (2021).
- ⁵²M. Andrychowicz, L. Espeholt, D. Li, S. Merchant, A. Merose, F. Zyda, S. Agrawal, and N. Kalchbrenner, “Deep learning for day forecasts from sparse observations,” (2023), arXiv:2306.06079 [physics.ao-ph].
- ⁵³S. C. Park, M. K. Park, and M. G. Kang, “Super-resolution image reconstruction: a technical overview,” *IEEE Signal Processing Magazine* **20**, 21–36 (2003).
- ⁵⁴T. Hastie, R. Tibshirani, and J. Friedman, *The Elements of Statistical Learning: Data Mining, Inference, and Prediction*, Springer series in statistics (Springer, 2009).
- ⁵⁵S. J. Fletcher, “Chapter 25 - applications of data assimilation in the geosciences,” in *Data Assimilation for the Geosciences (Second Edition)*, edited by S. J. Fletcher (Elsevier, 2023) second edition ed., pp. 1019–1065.
- ⁵⁶T. W. David, D. P. Marshall, and L. Zanna, “The statistical nature of turbulent barotropic ocean jets,” *Ocean Modelling* **113**, 34–49 (2017).
- ⁵⁷G. K. Vallis, “Effects of rotation and stratification,” in *Atmospheric and Oceanic Fluid Dynamics: Fundamentals and Large-Scale Circulation* (Cambridge University Press, 2017) p. 55–104.
- ⁵⁸G. K. Vallis, “Barotropic and baroclinic instability,” in *Atmospheric and Oceanic Fluid Dynamics: Fundamentals and Large-Scale Circulation* (Cambridge University Press, 2017) p. 335–378.
- ⁵⁹C. Canuto, M. Y. Hussaini, A. Quarteroni, and T. A. Zang, “Fundamentals of spectral methods for pdes,” in *Spectral Methods in Fluid Dynamics* (Springer Berlin Heidelberg, Berlin, Heidelberg, 1988) pp. 76–93.
- ⁶⁰M. Lin and C. Yang, “Ocean observation technologies: A review,” *Chinese Journal of Mechanical Engineering* **33**, 1–18 (2020).

- ⁶¹S. J. Fletcher, “Chapter 14 - observations,” in *Data Assimilation for the Geosciences (Second Edition)*, edited by S. J. Fletcher (Elsevier, 2023) second edition ed., pp. 601–629.
- ⁶²A. Paszke, S. Gross, F. Massa, A. Lerer, J. Bradbury, G. Chanan, T. Killeen, Z. Lin, N. Gimeshein, L. Antiga, A. Desmaison, A. Kopf, E. Yang, Z. DeVito, M. Raison, A. Tejani, S. Chilamkurthy, B. Steiner, L. Fang, J. Bai, and S. Chintala, “Pytorch: An imperative style, high-performance deep learning library,” in *Advances in Neural Information Processing Systems 32*, edited by H. Wallach, H. Larochelle, A. Beygelzimer, F. d'Alché-Buc, E. Fox, and R. Garnett (Curran Associates, Inc., 2019) pp. 8024–8035.
- ⁶³J. Kim, J. K. Lee, and K. M. Lee, “Accurate image super-resolution using very deep convolutional networks,” in *2016 IEEE Conference on Computer Vision and Pattern Recognition (CVPR)* (2016) pp. 1646–1654.
- ⁶⁴W. Shi, J. Caballero, F. Huszar, J. Totz, A. P. Aitken, R. Bishop, D. Rueckert, and Z. Wang, “Real-time single image and video super-resolution using an efficient sub-pixel convolutional neural network,” in *2016 IEEE Conference on Computer Vision and Pattern Recognition (CVPR)* (IEEE Computer Society, Los Alamitos, CA, USA, 2016) pp. 1874–1883.
- ⁶⁵K. He, X. Zhang, S. Ren, and J. Sun, “Deep residual learning for image recognition,” in *2016 IEEE Conference on Computer Vision and Pattern Recognition (CVPR)* (IEEE Computer Society, Los Alamitos, CA, USA, 2016) pp. 770–778.
- ⁶⁶A. L. Maas, A. Y. Hannun, A. Y. Ng, *et al.*, “Rectifier nonlinearities improve neural network acoustic models,” in *Proc. icml*, Vol. 30 (Atlanta, Georgia, USA, 2013) p. 3.
- ⁶⁷H. Hersbach, B. Bell, P. Berrisford, S. Hirahara, A. Horányi, J. Muñoz-Sabater, J. Nicolas, C. Peubey, R. Radu, D. Schepers, A. Simmons, C. Soci, S. Abdalla, X. Abellan, G. Balsamo, P. Bechtold, G. Biavati, J. Bidlot, M. Bonavita, G. De Chiara, P. Dahlgren, D. Dee, M. Diamantakis, R. Dragani, J. Flemming, R. Forbes, M. Fuentes, A. Geer, L. Haimberger, S. Healy, R. J. Hogan, E. Hólm, M. Janisková, S. Keeley, P. Laloyaux, P. Lopez, C. Lupu, G. Radnoti, P. de Rosnay, I. Rozum, F. Vamborg, S. Villaume, and J.-N. Thépaut, “The era5 global reanalysis,” *Quarterly Journal of the Royal Meteorological Society* **146**, 1999–2049 (2020), <https://rmets.onlinelibrary.wiley.com/doi/pdf/10.1002/qj.3803>.
- ⁶⁸Y. KOSAKA, S. KOBAYASHI, Y. HARADA, C. KOBAYASHI, H. NAOE, K. YOSHIMOTO, M. HARADA, N. GOTO, J. CHIBA, K. MIYAOKA, R. SEKIGUCHI, M. DEUSHI, H. KAMAHORI, T. NAKAEGAWA, T. Y. TANAKA, T. TOKUHIRO, Y. SATO, Y. MATSUSHITA, and K. ONOGI, “The jra-3q reanalysis,” *Journal of the Meteorological Society of Japan. Ser. II* **102**,

- 49–109 (2024).
- ⁶⁹S. Rasp, “Coupled online learning as a way to tackle instabilities and biases in neural network parameterizations: general algorithms and lorenz 96 case study (v1.0),” *Geoscientific Model Development* **13**, 2185–2196 (2020).
- ⁷⁰D. P. Kingma and J. Ba, “Adam: A method for stochastic optimization,” (2015).
- ⁷¹I. Higgins, L. Matthey, A. Pal, C. Burgess, X. Glorot, M. Botvinick, S. Mohamed, and A. Lerchner, “beta-VAE: Learning basic visual concepts with a constrained variational framework,” in *International Conference on Learning Representations* (2017).
- ⁷²A. Alemi, B. Poole, I. Fischer, J. Dillon, R. A. Saurous, and K. Murphy, “Fixing a broken ELBO,” in *Proceedings of the 35th International Conference on Machine Learning*, Proceedings of Machine Learning Research, Vol. 80, edited by J. Dy and A. Krause (PMLR, 2018) pp. 159–168.
- ⁷³A. Asperti and M. Trentin, “Balancing reconstruction error and kullback-leibler divergence in variational autoencoders,” *IEEE Access* **8**, 199440–199448 (2020).
- ⁷⁴Z. Wang, A. Bovik, H. Sheikh, and E. Simoncelli, “Image quality assessment: from error visibility to structural similarity,” *IEEE Transactions on Image Processing* **13**, 600–612 (2004).
- ⁷⁵G. Evensen, “Sequential data assimilation with a nonlinear quasi-geostrophic model using monte carlo methods to forecast error statistics,” *Journal of Geophysical Research: Oceans* **99**, 10143–10162 (1994), <https://agupubs.onlinelibrary.wiley.com/doi/pdf/10.1029/94JC00572>.
- ⁷⁶G. Burgers, P. J. van Leeuwen, and G. Evensen, “Analysis scheme in the ensemble kalman filter,” *Monthly Weather Review* **126**, 1719 – 1724 (1998).
- ⁷⁷G. Gaspari and S. E. Cohn, “Construction of correlation functions in two and three dimensions,” *Quarterly Journal of the Royal Meteorological Society* **125**, 723–757 (1999), <https://rmets.onlinelibrary.wiley.com/doi/pdf/10.1002/qj.49712555417>.
- ⁷⁸J. S. Whitaker, T. M. Hamill, X. Wei, Y. Song, and Z. Toth, “Ensemble data assimilation with the ncep global forecast system,” *Monthly Weather Review* **136**, 463 – 482 (2008).
- ⁷⁹F. Lluís, P. Martínez-Nuevo, M. Bo Møller, and S. Ewan Shepstone, “Sound field reconstruction in rooms: Inpainting meets super-resolution,” *The Journal of the Acoustical Society of America* **148**, 649–659 (2020), https://pubs.aip.org/asa/jasa/article-pdf/148/2/649/15344686/649_1_online.pdf.
- ⁸⁰R. Maulik, K. Fukami, N. Ramachandra, K. Fukagata, and K. Taira, “Probabilistic neural networks for fluid flow surrogate modeling and data recovery,” *Phys. Rev. Fluids* **5**, 104401 (2020).

- ⁸¹K. Gundersen, A. Oleynik, N. Blaser, and G. Alendal, “Semi-conditional variational auto-encoder for flow reconstruction and uncertainty quantification from limited observations,” *Physics of Fluids* **33**, 017119 (2021), https://pubs.aip.org/aip/pof/article-pdf/doi/10.1063/5.0025779/15872101/017119_1_online.pdf.
- ⁸²Y. Wang, X. Shi, L. Lei, and J. C.-H. Fung, “Deep learning augmented data assimilation: Reconstructing missing information with convolutional autoencoders,” *Monthly Weather Review* **150**, 1977 – 1991 (2022).
- ⁸³N. Aloysius and M. Geetha, “A review on deep convolutional neural networks,” in *2017 International Conference on Communication and Signal Processing (ICCSP)* (2017) pp. 0588–0592.
- ⁸⁴S. Ouala, R. Fablet, C. Herzet, B. Chapron, A. Pascual, F. Collard, and L. Gaultier, “Neural network based kalman filters for the spatio-temporal interpolation of satellite-derived sea surface temperature,” *Remote Sensing* **10** (2018), 10.3390/rs10121864.
- ⁸⁵H. W. Xie, D. Sujono, T. Ryder, E. B. Sudderth, and S. Allison, “A framework for variational inference and data assimilation of soil biogeochemical models using state space approximations and normalizing flows,” (2023), working paper or preprint.
- ⁸⁶K. He, X. Zhang, S. Ren, and J. Sun, “Delving deep into rectifiers: Surpassing human-level performance on imagenet classification,” in *Proceedings of the IEEE International Conference on Computer Vision (ICCV)* (2015).